University of Stavanger

Faculty of Science and Technology

MASTER'S THESIS

Study program/Specialization: Petroleum Engineering	Spring semester, 2018 Open
Author: Huong Lan Huynh	 .... (signature of author)
Supervisor: Prof. Zhixin Yu	
Title of master's thesis: Synthesis, characterization, and activity of bimetallic Ni-Fe hydrotalcite-derived catalysts in dry reforming of methane	
Credits (ECTS): 30	
Key words: Dry reforming of methane Syngas Hydrotalcite Ni-based catalysts Coprecipitation Fast injection Catalyst characterization	Number of pages: 67 Stavanger, 15/06/2018

ACKNOWLEDGEMENTS

ABSTRACT

The extensive amount of carbon dioxide (CO_2) emitted into atmosphere is arguably considered to be the main reason for global climate change due to the greenhouse effect. For decades, considerable efforts have been devoted to address this issue. Amongst the proposed solutions, dry reforming of methane (DRM) using CO_2 as feedstock for syngas production emerges as a promising alternative. DRM reaction utilizes two major greenhouse gases, methane (CH_4) and CO_2, and converts them into valuable syngas with hydrogen and carbon monoxide product ratio (H_2/CO ratio) close to unity, a desirable intermediate for a wide range of chemicals synthesis.

Heterogeneous catalysts are commonly used for the DRM reaction; however, the development of active and stable catalysts is still challenging. The noble metals (e.g. Rh, Pt, Ir, Pd and Ru) exhibit excellent catalytic activity and stability for DRM reactions, but the high cost and limited availability prevent their industrial application. Transition metals (e.g. Ni, Co) have good catalytic performance but suffer from fast deactivation due to carbon deposition and metal sintering. Recently, Ni-based hydrotalcite-derived (HT) materials have been proposed as promising or DRM reaction.

In this study, a series of bimetallic Ni-Fe catalysts supported on $MgAl_2O_4$ were prepared via HT precursors. The Ni loading was kept constant at 20 wt.% for all the catalysts while Fe content was varied by different Fe/Ni molar ratios. Two different coprecipitation methods were studied, namely conventional method (low supersaturation) and fast injection method (high supersaturation). The characteristics of catalysts were investigated by X-ray diffraction, nitrogen adsorption-desorption, hydrogen chemisorption, temperature programmed reduction and temperature programmed desorption. The HT-like materials were successfully synthesized with high crystallinity and porosity; small Ni-Fe alloy particles were highly dispersed and homogeneously distributed after the calcination of the precursors. The addition of Fe improved the reducibility and basicity of the catalyst. The advantage of fast injection method was demonstrated by that the catalyst possessing higher surface area, narrower size distribution, enhanced reducibility, and higher basicity.

The catalytic performance towards DRM reaction was studied in a fixed-bed reactor at 700 °C and atmospheric pressure. An equimolar CH_4/CO_2 feed at high gas hourly space velocity (GHSV) of 240,000 $mL.g^{-1}.h^{-1}$ was used. Ni-based catalyst with a small addition of Fe exhibited better performance than monometallic catalysts. The optimal composition was found at an Fe/Ni molar ratio of 0.1. A higher reduction temperature was also tested. Interestingly, a high and stable conversion of CH_4 and CO_2 during 18 hours of time on stream was achieved by the catalyst synthesized by fast injection method. The synthesis of small and uniform Ni-Fe alloy particles could be an effective approach to improve catalytic activity and stability against carbon formation and sintering for DRM reaction toward commercialization.

TABLE OF CONTENTS

LIST OF TABLES

LIST OF FIGURES

1. INTRODUCTION

1.1. Background

As the rapid development of the industry, transport and human society in this modern world, the demand of energy is steadily growing. Every year, the global primary energy consumption increases at an average rate of 1.8% [1]. Accounting for a third of the energy consumption, oil remains as the world's leading fuel, yet increasing in a slower rate. The focus is shifting to natural gas, a cheaper and greener source of energy. With a total proven reserves of 187 trillion cubic meters, only 1.9% of the natural gas source has been produced around the world. According to British Petroleum's Energy Outlook 2018, natural gas grows much faster than either oil and coal [2].

In a close relationship, as the climb in the consumption of fossil fuel, the amount of produced carbon dioxide (CO_2), the primary greenhouse gas that harms the Earth's atmosphere, is increasing spontaneously. Methane (CH_4) from natural gas, also a greenhouse gas, is initially far more devastating to the climate than CO_2 because of its highly effective heat absorption.

CH_4 is a reducing agent whilst CO_2 is one of the most common oxidizing agent [3]. Finding a solution utilizing two carbon-based feedstocks and mitigating the environmental impact of greenhouse gas emissions is therefore of essence. Dry reforming of methane (DRM), involving the simultaneous valorization of both gases, is one of the most attractive processes to achieve the goals. It has gained considerable attention since Fischer and Tropsch firstly investigated the reaction in 1928 [4]. The products of DRM reaction are hydrogen (H_2) and carbon monoxide (CO), called as synthetic gas (syngas), which are highly valuable building blocks for synthetic fuels and chemicals production. Moreover, DRM reaction can be extended to biogas (CO_2 and CH_4) upgrading and utilization, an environmental-friendly fuel feedstock [5].

The development of DRM catalysts has been a challenge for decades. The aim is to synthesis highly active and stable catalysts with high resistance to deactivation caused by carbon deposition, metal sintering, etc. Nickel-based materials are the most investigated catalysts for DRM reaction, despite the outstanding performance of noble-metal-based catalysts. Nickel (Ni) catalysts are widely used in industrial scale since it is more economically available. Reports showed that Ni-based catalysts with a suitable support [6] or the alloying with other metals as active sites improved the catalytic activity and suppressed carbon formation in DRM reaction [7, 8].

Hard-to-reduce oxides, alumina (α-Al_2O_3) and magnesia (MgO) are widely used as supports for nickel catalysts [4]. Interestingly, the mixed MgO-Al_2O_3 supports performed the beneficial effects from both oxides. The mixed oxides support enhanced the chemisorption of CO_2 and the thermal stability due to magnesia and alumina, respectively. On the other hand, an effective approach considering the

addition of a secondary metal to Ni has been proposed recently to further improve its catalytic activity and stability. The use of iron (Fe) became a promising solution, due to its significantly low cost and high availability, despite contradictory reports on the role of Fe [7].

Preparation method significantly influences the properties of catalysts in DRM reaction. Ni-based catalysts from hydrotalcite-like precursors has received much attention for their outstanding properties. Hydrotalcite (HT), a double-layered hydroxides material, has unique structure, versatility in composition, tunable properties, etc., offerings an enormous potential in the design and synthesis of novel supported catalysts. The two or more different divalent and trivalent metal cations are homogeneously dispersed in brucite-like layers of HT materials [9]. The mixed oxides derived from HT precursors possess high surface area, basic surface properties and high structural stability.

1.2. Scope of the study

The objective of this work was to study the catalytic activity and stability of bimetallic Ni-Fe HT-derived catalysts synthesized by different methods in DRM reaction. The effect of reduction temperature on the structure and activity of the catalysts were also investigated.

A series of bimetallic Ni-Fe HT-derived catalysts with varied Fe/Ni molar ratio (from 0 to 1) were prepared by conventional method (coprecipitation at low supersaturation) and fast injection method (coprecipitation at high supersaturation). The catalysts were characterized by X-ray diffraction (XRD), nitrogen adsorption-desorption, hydrogen chemisorption, temperature programmed reduction (TPR) and temperature programmed desorption (TPD). The catalysts were tested in DRM reaction at a temperature of 700 ^{o}C, a pressure of 1 bar and a high gas hourly space velocity (GHSV) of 240,000 mL.g^{-1}.h^{-1}.

2. LITERATURE REVIEW

2.1. Methane reforming technologies

Reforming of methane is the most extensive industrial route for syngas production. Particularly, there are several approaches, such as steam reforming, partial oxidation, autothermal reforming, as well as dry reforming process. Table 2.1 summaries the main reactions for different reforming technologies.

Table 2.1. Main reactions of different reforming processes

Processes	Reaction	ΔH_{298K} (kJ/mol)
Steam Reforming of Methane (SRM)	$CH_4 + H_2O \leftrightarrow CO + 3H_2$	+228
Partial Oxidation of Methane (POM)	$CH_4 + \frac{1}{2} O_2 \leftrightarrow CO + 2H_2$	-23
Dry Reforming of Methane (DRM)	$CH_4 + CO_2 \leftrightarrow 2CO + 2H_2$	+247

Different type of oxidants is used in the processes, which results in the varied ratio of produced H_2 and CO. The production of syngas is thermodynamically favored by a system consumes oxygen (O_2). However, due to technical and economic problems, pure O_2 is not preferable in the industrial scale while a mixture of O_2, steam and/or CO_2 are commonly used. Furthermore, when CO_2 and H_2O were added to the feed, the H_2/CO ratio in the output gas is suitable for downstream processes such as ammonia and methanol synthesis. In contrast to POM, SRM are highly endothermic (as shown in Table 2.1) and produces syngas with the highest H_2/CO ratio of three. The process is also energy intensive and requires high capital expenditure [3].

DRM reaction is not as thermodynamically favorable compared to the other processes. However, its potential for the utilization of CO_2 has received much attention, giving an environmental-friendly approach for the reduction of carbon footprint. Researchers are focusing on the exploration of effective catalytic systems to overcome thermodynamic barrier and catalyst deactivation, which are the challenges hindering the commercialization of the DRM process. H_2 and CO produced from DRM with a ratio of unity can be used directly for oxygenated chemicals production [10].

2.2. DRM reaction thermodynamics

The main and side reactions in DRM process are shown in Table 2.2 [11]. The thermodynamic behavior of DRM reaction is crucial to define suitable operating conditions such as temperature, pressure, and feed ratio to obtain high conversion and yield. In addition, catalyst deactivation caused by carbon deposition is a major concern in DRM process. Therefore, the study of carbon formation

boundary provides fundamentals to design suitable operating conditions which can prolong the catalyst lifetime.

Table 2.2. Primary and side reactions in dry reforming of methane

Reaction	Equation	ΔH_{298K} (kJ/mol)	T ($^{\circ}$C) $\Delta G_T \leq 0$
Dry reforming of methane (DRM)	$CH_4 + CO_2 \leftrightarrow 2CO + 2H_2$	+247	≥ 643
Reverse water-gas shift (RWGS)	$CO_2 + H_2 \leftrightarrow CO + H_2O$	+41	≥ 827
CH_4 decomposition	$CH_4 \leftrightarrow C + 2H_2$	+75	≥ 546
CO disassociation (Boudouard reaction)	$2CO \leftrightarrow C + CO_2$	-171	≤ 703
CO_2 gasification	$C + CO_2 \leftrightarrow 2CO$	+171	≥ 703
Carbon water reaction (CW)	$C + 2H_2O \leftrightarrow 2H_2 + CO$	+90	≥ 631

According to the thermodynamic principles, the endothermic DRM reaction requires a large amount of energy input. Reaction occurs at above 643 $^{\circ}$C, the turning temperature point for Gibbs free energy changes to negative. CH_4 decomposition and CO disassociation (Boudouard reaction) are the main reactions producing carbon. From a thermodynamic perspective, these reactions can be alleviated by operating outside the temperature range of 546-703 $^{\circ}$C. At temperatures higher than 703 $^{\circ}$C, CO_2 gasification reaction also takes place, which consumes deposit carbon. Water in the reaction system are formed from Reverse Water-Gas Shift (RWGS) reaction, which is endothermic and favorable at the temperature over 827 $^{\circ}$C.

The thermodynamic analysis of DRM based on the total Gibbs free energy minimization of multi-reaction system has been reported by Cao *et al.* [11]. The pressure was studied at 1 bar and CH_4/CO_2 molar ratio was fixed at one. The calculated equilibrium conversion of CH_4 is 91% as seen in Fig. 2.1. These data was also similar with Nikoo and Amin's study [12].

The effect of pressure and CH_4/CO_2 ratio on DRM were also studied. Based on Le Chatelier's principle, high pressures were unfavorable for reactant conversions. Lower CH_4/CO_2 positively influenced CH_4 conversion but had negative impact on CO_2 conversion, as CH_4 played the role of a limiting reactant, resulting in a lower CO_2 conversion [12]. The appropriate operating conditions concluded from the analysis were high temperature (>1000 $^{\circ}$C), unity reactant molar ratio, and atmospheric pressure to avoid carbon formation regime [11].
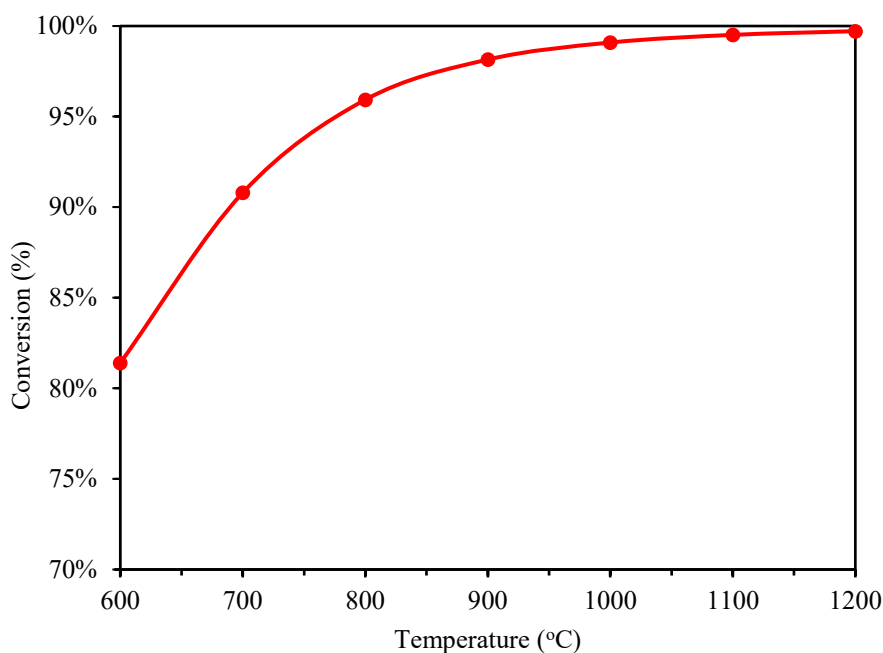
Figure 2.1. Calculated equilibrium conversion of CH_4 in DRM (P=1 bar, CH_4:CO_2 = 1:1)

2.3. DRM catalysts

2.3.1. Nickel-based catalysts

The catalysts for DRM reaction are supported catalyst with noble metals (e.g. Ru, Rh, Pt, Pd, etc.) and transitional metal (e.g. Ni, Co, Fe). Noble metals exhibit excellent catalytic activity and stability due to their superb carbon resistance. However, it is not economically attractive for industrial scale due to high cost and limited availability. Ni-based catalysts are widely used for commercial processes since it is cheaper and more available with good catalytic performance.

The major concern of Ni-based catalysts is low coke resistance which has been investigated by many research groups since the last decade. The principle of carbon formation on Ni surface has been extensively studied. Reports shown that whisker carbon was mainly formed via CH_4 decomposition and CH_4 promoted the aggregation of Ni more dramatically than CO [13, 14].

The particle size of nickel is a crucial factor in carbon deposition. Ni particles, particularly in supported catalysts, can easily agglomerate due to thermal sintering, because of its low Tammann temperature (the temperature when atoms of bulk become increasingly mobile, at about 600 °C for Ni [15]). Chen *et al.* studied the effect of the crystal size of Ni on the growth of carbon nanofibers and reported that smaller Ni crystals had lower coking rate [16]. Bychkov *et al.* also reported that the rate of carbon accumulation was increased with the increase of Ni particle size in DRM reaction [17].

Efforts have been spent to improve the performance and lifetime of Ni-based catalysts, by studying supports, promoters, multi-metal as active sites, etc. Preparation methods and pretreatment process also affect the structural properties, reduction behavior and catalytic performance.

2.3.2. Catalyst supports

Support is an important component of a catalyst, constructing the catalyst into desired shape and structure [18]. By having a large surface area, support material can facilitate the dispersion and surface area of metal species when embedding the active metal in. Generally, supports are inactive in catalytic reactions.

According to Guo *et al.*, suitable supports will maintain the metal dispersion of the catalysts and be resistant to high operating temperature [6]. Ni catalysts with different supports were studied and showed that compared to $Ni/\gamma-Al_2O_3$, $Ni/MgO-\gamma-Al_2O_3$ and $Ni/MgAl_2O_4$ catalysts exhibited higher activity and stability in DRM process. $MgAl_2O_4$ spinel can stabilize Ni crystallites and enhance the resistance towards coking and sintering.

Min *et al.* [19] also reported that the addition of MgO to Al_2O_3 resulted in a better resistance to coke formation, increased interaction between NiO and support, as well as the increase of basicity and CO_2 adsorption. With a small amount of MgO added, less active and less stable $NiAl_2O_4$ was formed. At moderate addition of MgO, the formation of $MgAl_2O_4$ spinel favored the reduction of Ni particles and increased the specific surface area of the catalyst. When MgO content was high, NiO-MgO solution was obtained which was hard to be reduced but increased the activity in DRM reaction [19]. Moreover, the preparation method of supported catalysts was proved to have influence on catalytic performance. Coprecipitated catalyst with larger crystallite size was deactivated faster than catalysts with smaller crystallite size prepared by sol-gel method, which was due to Ni sintering [19]. Another strategy to avoid agglomeration and larger particles is to enhance metal-support interaction to maintain high metal dispersion [20], keeping small particle size to eliminate Ni metal sintering [21].

2.3.3. Bimetallic Ni-based catalysts

Alloying nickel with other metals can influence the catalyst structure and consequently the catalytic activity. For example, the synergistic effect of Ni-based bimetallic surface could decrease the C adsorption energy, hence lower the affinity for carbon deposition and improve the coke resistance of the catalyst [22]. Since noble metals have excellent catalytic activity and better carbon resistance, many researches have investigated in their small addition to Ni catalysts. A significant increase in both activity and carbon resistance has been reported [23]. However, besides noble metals, transition

metals such as Fe, Co, and Cu, etc., have also been investigated as bimetallic system with Ni-based catalysts for DRM process.

Fe monometallic catalysts are inactive for DRM; however, Ni-Fe bimetallic catalysts have shown higher conversion and better stability than monometallic catalyst Ni. Fe is one hundred times cheaper than Ni [24], hence it becomes an economically attractive candidate to improve Ni-based catalysts for DRM. According to literature, many Ni-Fe bimetallic catalysts are derived from specific structure like perovskite and spinel. Ni ferrite and HT have also drawn much attention as catalyst precursors. Tomishige *et al.* used HT as precursors and found that the formation of uniform Ni-Fe alloy nanoparticles, resulting from homogeneous distribution of metal ions, are accounted for their high catalytic activity in the steam reforming of tar [25-27].

According to Theofanidis *et al.*, Ni/Fe molar ratio strongly influenced the role of Fe in the activity of Ni-Fe/$MgAl_2O_4$ catalyst for DRM. Ni-Fe alloy was found to remain stable after reduction, while metallic Fe segregated from the alloy to form FeO_x in the presence of CO_2. The alloy decomposed into Ni and Fe_3O_4 at above 900K (627 °C) for 0.7-Fe/Ni catalyst (with Fe/Ni molar ratio of 0.7).

In a good agreement with Theofanidis's study, a series of HT-derived Ni-Fe catalysts supported on $MgAl_2O_4$ also showed an increase in activity and stability in DRM, especially for the catalyst with Fe/Ni molar ratio of 1/3 [7]. The adsorption energy values and DRM energetics on the surface of Ni and Ni_3Fe_1 catalysts have been calculated by density function theory (DFT). It has been concluded that oxygen binding was more favorable for Ni_3Fe_1 due to stronger Fe-O interaction. While CH_4 activation activity was comparable between the two catalysts, Ni_3Fe_1 alloy surface activated CO_2 more easily. Because of that, a larger amount of lattice oxygen (O*) was yielded to partially oxidizes deposit carbon (formed by CH_4 decomposition and/or Boudouard reaction) into CO (C* + O* $\rightarrow$ CO). This effect also induced the changes in alloy structure. Partial dealloying of Ni-Fe and the formation of FeO during DRM have been proved by operando X-ray absorption spectroscopy and X-ray diffraction (XAS-XRD) and scanning transmission electron microscopes – energy-dispersive X-ray spectroscopy (STEM-EDX). In addition, during DRM reaction, the oxidation of Ni was not observed, which led to further hypothesis that catalyst deactivation was due to carbon formation, not the formation of NiO, Ni_3C, or $NiAl_2O_4$, nor sintering.

2.3.4. Layered double hydroxides

Layered double hydroxides (LDHs), also known as anionic clays, or HT-like materials since its structure are analogous to that of HT, a natural magnesium-aluminum hydroxycarbonate. It is a large group of natural and synthetic materials which can be easily synthesized by the exposure of metal salts mixture to base. Due to a wide range of potential applications such as catalysts and supports,

anion scavenger for water treatment, electroactive and photoactive materials, etc., this group of clay materials has been investigated by many scientists around the world [28].

The general formula for LDHs material is $\left[M_{1-x}^{2+} M_x^{3+} (OH)_2 \right]^{x+} A_{x/n}^{n-} . m H_2 O$, where M represents metals, A for anion. The value of x is preferred to be in the range of 0.2 to 0.4 to obtain a pure LDH phase and avoid the formation of hydroxides and other compounds. As mentioned, divalent cations can be Mg and/or other metals (e.g. Fe, Co, Cu, Ni, or Zn); trivalent cations are Al and/or other metals (e.g. Cr, Ga, In, Mn or Fe). The only requirement is that their radii for octahedral coordination should be indifferent to those of Mg^{2+} and Al^{3+}.

LDHs are composed of brucite-like layers, as illustrated in Fig 2.2 [29]. Using $[Mg_3Al(OH)_8][(CO_3)_{1/2}.2H_2O]$ as a representative, it is closely related to that of brucite $Mg(OH)_2$ [30]. Each Mg^{2+} ion is octahedrally bonded to six OH^- ions. Each octahedra shares edges with others to form an infinite two-dimensional brucite layer. Partial replacement of Mg^{2+} ions by Al^{3+} gives the brucite-like layers a positive charge, which is balanced by carbonate anions located in the interlayer region between the two layers. Water molecules and hydrogen bonds are also existing in this interlayer region, together with the electrostatic interactions hold the layers together, forming the three-dimensional structure. Synthetic LDHs are usually in rhombohedral (3R) polytypes. On the other hand, the electric charge of the layers and interlayer ions are just opposite to silicate clays (cationic clays). Hence, it is reasonable to call this material as anionic clays [28].
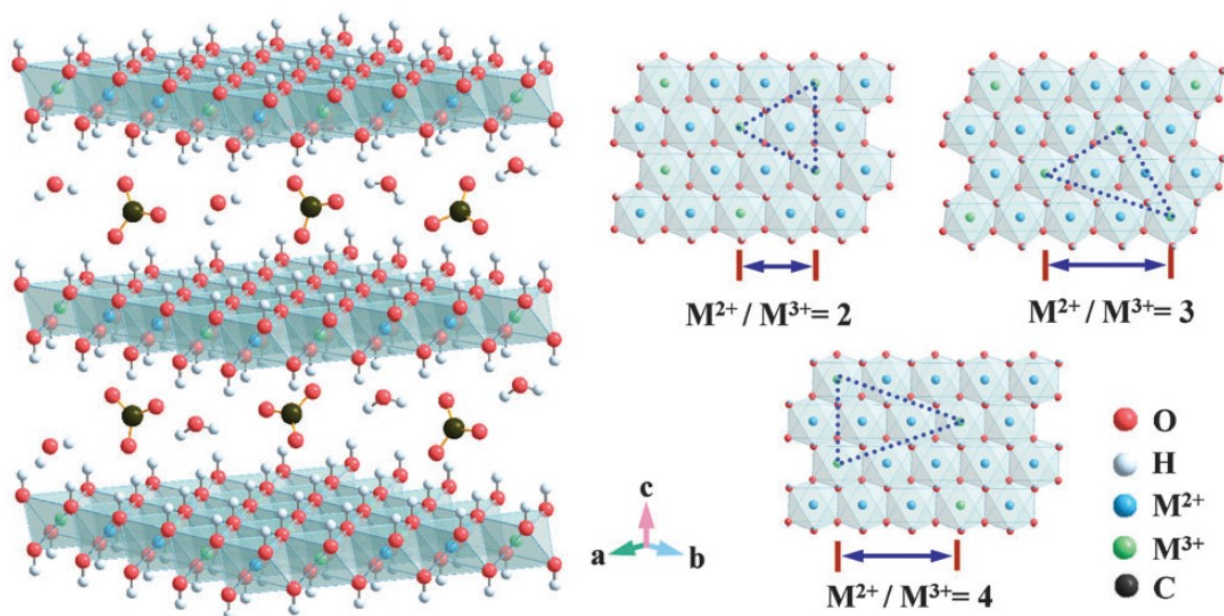
Figure 2.2. The idealized structure of carbonate-intercalated LDHs with different M^{2+}/M^{3+} molar ratios [29]

Interest in HT arises from the wide range of choice of cations and anions to make this material a suitable heterogeneous catalyst for various reactions. As the cations in HT are well dispersed, the obtained mixed oxides upon thermal decomposition usually show high distribution of metal active sites. Therefore, derivatives of LDHs after calcination are often used as supported metal catalyst, as illustrated in Fig. 2.3 [29].
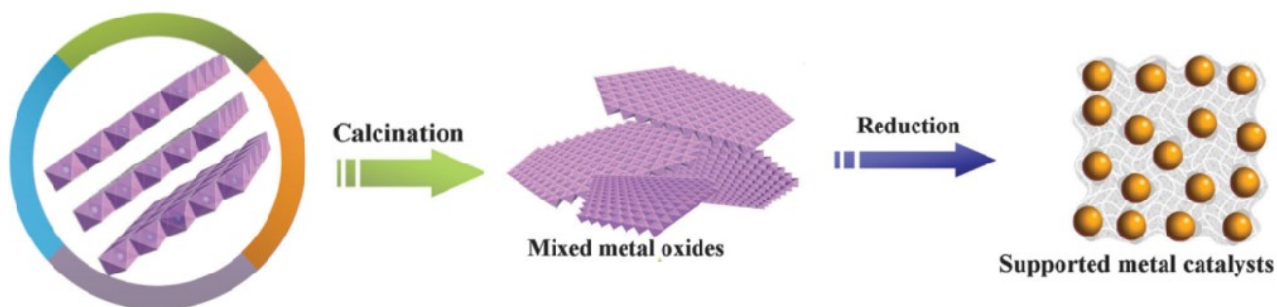
Figure 2.3. Synthetic pathway for the preparation of the LDH-based catalysts [29]

An important feature is that the basic strength of the support from LDHs can be flexibly tuned by changing metal compositions to achieve suitable activity and selectivity for specific catalytic reactions. By taking advantages of this, LDHs have been intensively studied for various catalytic reaction, including hydrogenation and hydrodesulfurization, polymerizations, and particularly syngas production from steam reforming.

In this study, Ni and Fe bimetallic alloys were proposed as potential catalyst for DRM. According to reported data, Ni and Fe can be used as replacing metals because of the close ionic radii to either Mg^{2+} or Al^{3+} (as shown in Table 2.3), which are expected to be able to be incorporated simultaneously into the brucite-like layers of LDHs.

Table 2.3. Ionic radii of cations with coordinate number of 6 [31]

M^{2+}	Radius (nm)	M^{3+}	Radius (nm)
Mg	0.072	Al	0.054
Ni	0.069	Fe	0.055

2.3.5. Catalyst synthesis

Besides indirect synthesis methods such as anion exchange within an LDH precursor, sol-gel techniques, etc., direct synthesis via coprecipitation is the most common preparation method of HT materials. To obtain a pure HT, different synthesis parameters have been identified, such as the ratio

of cations and anions, anion introduced in higher concentration in the solution to ensure pillaring [9], total concentration of cationic solution to be 0.5 M or less to form a gel [32].

2.3.5.1. Coprecipitation

HT materials are mostly prepared by direct synthesis, which involves nucleating and growing of metal hydroxide layer by mixing an aqueous solution of two metallic salts in a desired anion and a base. A drawback of this technique is that it can be used only if the desired interlayer anion is held as strongly as the counterion in the metal salts used. Because of that, metal nitrates and metal chlorides are widely used [32].

Moreover, to prevent the aggregation of poor crystallinity, one refinement is precipitation at a constant pH, referred to as coprecipitation. It is suggested that all the cations precipitate simultaneously in a fixed ratio. The steady addition of a cationic solution into a base solution under vigorous mixing is required. The pH chosen must ensure that it is necessary for LDH formation, but it should also be lower than the required precipitation pH of divalent metal hydroxide itself [32]. It is reported that Fe (III), Al (III), Ni (II) precipitates at pH 6-9, pH 6 and pH 10.2, respectively [33]. The pH of the solutions should preferably be higher than pH 7 and less than pH 10 [34].

Three methods of precipitation have been reported [9]. In this study, two methods, i.e. coprecipitation at low supersaturation and high supersaturation at constant pH are investigated. The difference between the two methods is that the cationic solution was added rapidly for high supersaturation (e.g. fast injecting by syringe [35]), and slowly for low supersaturation (e.g. dropping within 2 hours [34]).

Coprecipitation at low supersaturation is commonly used in the preparation of HT materials. After mixing the solutions at certain constant pH and temperature, washing is carried out and followed by aging procedure. Drying temperature should not exceed 120 °C. The prepared materials have more crystalline precipitates.

Coprecipitation at high supersaturation generally provides less crystalline materials, due to the high number of crystallization nuclei. It is reported that the rate of nucleation is higher than the rate of crystal growth. Hence, the prepared materials are amorphous precipitates [35].

2.3.5.2. Aging

Under conventional methods, LDHs are formed with poor crystallinity. Aging, a post-preparation treatment is normally used to alleviate this problem and to enhance the formation of well-crystallized LDH [36]. The step consists of stirring at room temperature or under heat with reflux. It presumably occurs through Ostwald ripening, in which larger crystallites grow at the expense of smaller particles in the solution [32].

It is worth mentioning that the temperature of aging affects grain size and morphology of the material. Wang *et al.* reported that large crystals with more perfect and regular hexagonal shape were formed when aging at increasing temperature (up to 90 $^{\circ}$C) due to the facilitated ion diffusion. Larger crystals were obtained with more energetically stable structure [37].

2.3.5.3.   Calcination

Calcination is a thermo-chemical treatment step where the as-prepared precursors are heated in the presence of oxygen or synthetic air under a defined temperature. After the treatment, hydroxide materials become mixed oxides with well dispersed cations. For LDH materials, this process typically involves dehydration, dehydroxylation, decomposition of anions and oxide reformation [9, 30], as represented in reactions below.

Dehydration: $\left[M_{1-x}^{2+}M_x^{3+}(OH)_2 \right]^{x+} A_{x/n}^{n-}.mH_2O \rightarrow \left[M_{1-x}^{2+}M_x^{3+}(OH)_2 \right]^{x+} A_{x/n}^{n-}$

Dehydroxylation: $\left[M_{1-x}^{2+}M_x^{3+}(OH)_2 \right]^{x+} A_{x/n}^{n-} \rightarrow \left[M_{1-x}^{2+}M_x^{3+}O \right]^{x+} A_{x/n}^{n-}$

Decomposition of anion: $\left[M_{1-x}^{2+}M_x^{3+}O \right]^{x+} A_{x/n}^{n-} \rightarrow M_{1-x}^{2+}M_x^{3+}O_{1+x/2}\ (BO_y)$

Oxide reformation: $M_{1-x}^{2+}M_x^{3+}O_{1+x/2}\ (BO_y) \rightarrow M^{2+}O + M^{2+}M_2^{3+}O_4 + BO_y$
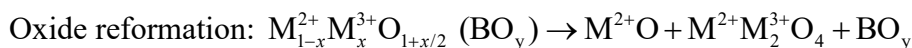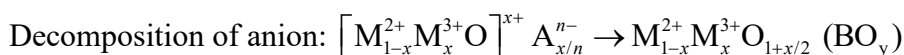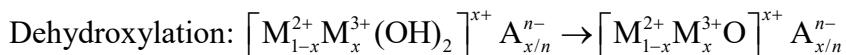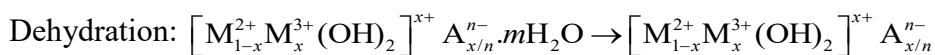
Where $M^{2+}O$ is an oxide with rock salt phase, $M^{2+}M^{3+}{}_2O_4$ is a mixed oxide with spinel phase, and BO_y denotes decomposed anion species. The dehydration undergoes at 100-250 $^{\circ}$C, followed by dehydroxylation at 350-450 $^{\circ}$C. The later steps of decomposition and oxidation occurs at 420-700 $^{\circ}$C. However, for LHDs containing oxidizable divalent cations, such as Co, Ni, Mn, an oxidation reaction spontaneously occurs during the heating. This facilitates the dehydroxylation to occur below 250-300 $^{\circ}$C. Moreover, rock salt oxide may not be formed, while pure spinel phase of mixed oxide is readily produced at low temperatures (e.g. 300 $^{\circ}$C) [30, 38]. It has been reported that the temperature of calcination influenced the average size of Ni particles and surface area [39].

2.3.5.4.   Reduction

Reduction is sometimes considered as pre-treatment step or activation step for catalytic reactions, where metal oxides are converted into active metallic species by using reducing agent, such as hydrogen. Hence, the catalysts are ready to perform their catalytic activities in the reaction. The most important variable in a reduction process is temperature, which affects the dispersion, metal surface area and extent of reduction of the catalysts. It is reported that high metal-loading catalysts are easier to reduce than the low metal-loading catalysts [40].

2.4. Catalyst characterization

2.4.1. X-ray diffraction (XRD)

X-ray diffraction method can provide information about the atomic structure of crystalline materials. Diffractogram, i.e. an x-ray powder diffraction pattern, shows the positions and intensities of a set of peaks, which can be compared to a database of materials in order to identify the contents of the sample and to determine the presence or absence of any particular phase [41].

When X-rays are directed toward the sample, stoked atom reflects many different waves including scattering waves. The relationship between the electromagnetic radiation wavelength λ, the spacing d between crystal lattice planes of atoms, and the angle of incidence θ is represented through eq. 2.1. following Bragg's law [42].

$$\lambda = 2 \times d \times \sin\theta \tag{2.1}$$

On the other hand, d - the crystallite size in the direction perpendicular to the lattice planes can be estimated by the Scherrer equation (eq. 2.2) [43].

$$d = \frac{K\lambda}{B\cos\theta} \tag{2.2}$$

Where K is a numerical factor referred as the crystallite-shape factor, B is the full width at half maximum of the XRD peak (in radians).

During the experiments, a beam of x-rays is allowed to impinge on the sample. These x-rays are generated by a cathode ray tube with a beam of electron radiating toward a metallic target (made of copper, molybdenum, etc.). The diffracted intensity as a function of angle is recorded. There are three main diffraction methods and powder method (PXRD) is the most common one using fixed wavelength. All possible diffraction directions of the lattice could be obtained due to the random orientation by scanning the sample through a range of 2θ angles. Copper is the most commonly used metallic target, and CuKα radiation wavelength is 1.5418 Å. For typical powder patterns, data is collected at 2θ angles from 5° to 70°.

Besides the identification of unknown material, there are numerous advantages and applications of PXRD such as polymorph study, variable temperature and relative humidity study, phase transition study, etc. [44]. In terms of determination of crystal structure and lattice parameters using PXRD, the position of diffraction pattern provides information about unit cell (size and shape) while the intensities can be used to examine the atom positions of the sample. By comparing the peak positions of XRD pattern with database, the sample can be defined. The peaks indicate the geometry of the

lattice, both dimensions and internal symmetries. This type of experiment is simple, rapid, and sufficient with average sample quality to solve the structure of an unknown material.

In addition, observing the relative intensities of the diffracted beams or more interestingly considering the integrated intensity, i.e. the relative area under the curve of intensity vs 2θ, can lead to the determination of atom arrangement and the comparison of crystallinity. There are many factors which can affect the intensity, such as the addition of atoms in the unit cell, the number of crystal oriented at or near the Bragg's angle, the regularity of the lattice as well as the periodicity and tendency to "order" of atoms [42].

2.4.2. Nitrogen adsorption-desorption

Gas adsorption-desorption is the most popular method available for the surface area and pore size characterization of porous materials. There are two types of adsorption: chemisorption and physisorption which are differentiated by the strength of the interaction. Physical adsorption is the most suitable approach for surface area measurement, because of its lower heat of adsorption without violent or disruptive structural changes to the surface during measurement. Unlike chemisorption, the surface is physically covered by more than one layer of adsorbate. Moreover, the equilibrium is rapidly achieved since no activation energy is required. Therefore, pores can be filled step by step from micropores to monolayer; then to multilayer or capillary condensation. Analyzing the adsorption and desorption data can result in the measurement of pore volume, pore size and distribution [45].

The Brunauer - Emmett - Teller (BET) theory is the most widely applied method to determine the surface area of porous materials. The kinetic theory was extended to multilayer adsorption, resulting in BET equation as eq. 2.3.

$$\frac{1}{W\left(\dfrac{P}{P_0}-1\right)} = \frac{1}{W_m C} + \frac{C-1}{W_m C}\left(\frac{P}{P_0}\right)$$

(2.3)

Where P and P_0 are the equilibrium and the saturation pressure of adsorbates at the temperature of adsorption; C is the BET constant related to the adsorbent and adsorbate interactions. By measurement, the accumulated gas quantity adsorbed versus gas pressure data at specific temperature (depending on adsorbate, i.e. 77K for nitrogen) is recorded and forms a graph of $1/[W \times (P/P_0 - 1)]$ versus P/P_0, which yields a straight line in the range of $0.05 < P/P_0 < 0.3$. W_m then can be solved and the specific surface area is calculated.

According to International Union of Pure and Applied Chemistry (IUPAC) classification, there are six sorption isotherms from type I to type VI, as shown in Fig. 2.4 and Fig. 2.5 [46]. For instance,

type IV isotherm is observed for mesopores materials, with a characteristic hysteresis loop and the limiting uptake over a range of high P/Po. Such hysteresis loops may exhibit a wide variety of shapes. This shape has often been correlated to the specific pore structure. Type H1 is often associated with porous materials consisting of agglomerates or compacts of uniform spheres in regular array with a narrow distribution of pore size. For type H2 porous adsorbents, it is more difficult to interpret.
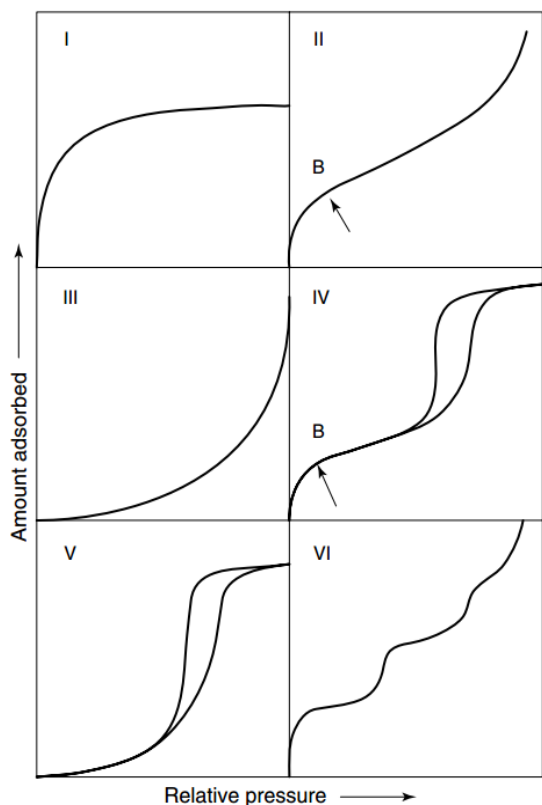
Figure 2.4. Types of physisorption isotherms [46]   Figure 2.5. Types of hysteresis loops [46]
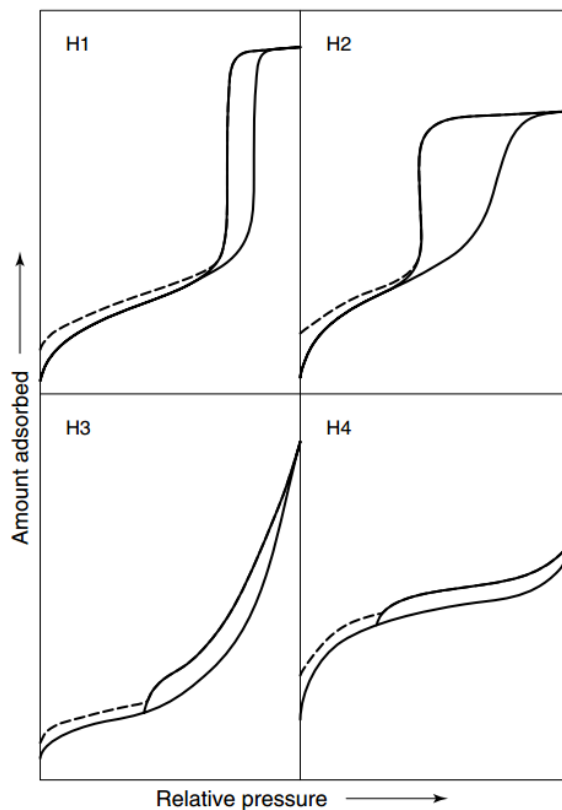
The BET theory is almost universally applied due to its simplicity, definitiveness, and its ability to accommodate the variety of isotherm types (from type I to type V). In addition, the BET theory and experimental isotherm are in good agreement in the region of relative pressure near completed monolayer, which made BET theory the most reliable method for surface area measurement. Nitrogen at 77K has been generally used as an international standard BET adsorbate because of its unique properties. In fact, nitrogen has a permanent quadrupole moment which is responsible for the formation of a well-defined monolayer on samples' surface.

Barrett-Joyner-Halenda (BJH) method is used to determine pore volume and pore size distribution, mainly applied for mesopores materials. The results are computed directly from the gas desorption isotherm and modified Kelvin equation. By relating vapor pressure depression to capillary radius, the relationship between volume of capillary condensate and relative pressure can be defined [47].

2.4.3. Hydrogen chemisorption

The method of gas chemisorption is best suited for the determination of exposed active sites since adsorbate molecule forms chemical bond on the surface of adsorbent [45]. By measuring the quantity of chemisorbed gas, the number of active sites on catalysts can be calculated from a simple association of one gas molecule with one exposed metal atom [45].

Experimentally, from the quantity of gas adsorbed by the sample, or isotherm, the monolayer capacity, V_m can be obtained. At low pressure, the surface of sample is saturated with chemisorbate and assured the formation of a monolayer. Additional physical adsorption occurs when pressure increases. By extrapolating back to zero pressure of the physisorption linear isotherm, V_m is acquired. However, when weak chemisorption is expected on the sample, a second repeat isotherm must be obtained to exclude the contribution of weak chemisorption [45]. After completing the first isotherm, weakly bonded gas molecules are desorbed at analysis temperature, hence only strongly bonded gas molecules remain. The second isotherm is conducted with the same procedure, consisting of only weak chemisorption and physisorption. The difference between the two isotherms gives irreversible isotherm, representing the amount of strong chemisorption.

Using Langmuir model, the active sites on the surface can be determined from the isotherm by eq. 2.4, where V_m (mL, at standard temperature and pressure) is the monolayer volume; L is Avogadro's number (6.022×10^{23}), S is adsorption stoichiometry factor (e.g. $S = 2$ for H_2 on Ni). The total active metal area A_m is expressed by eq. 2.5, where A_x is the cross-sectional area of metal atom. In the case of supported metal catalysts, dispersion $\gamma\%$, the percentage of exposed metal atoms to the total metal content (N_t), can be calculated by eq. 2.6.

$$N_a = \frac{V_m}{22414} LS \tag{2.4}$$

$$A_m = \frac{N_a A_x}{W} \tag{2.5}$$

$$\gamma\% = \frac{N_a}{N_t} \times 100\% \tag{2.6}$$

2.4.4. Temperature Programmed Reduction (TPR)

Temperature programmed reduction (TPR) is a method for the characterization of metal oxide, mixed metal oxides, and metal oxides dispersed on a support. The resulting TPR profile provides qualitative information on the oxidation state of the reducible species: number of reducible species, temperature at which the reduction occurs.

During the TPR, a reducing gas mixture, normally hydrogen in carrier gas, flows over the mixed oxide (MO) sample while the temperature increases linearly with time. When the gases react with the MO, metal (M) and water are formed, and hydrogen concentration decreases in the gas mixture.

$$MO + H_2 \rightarrow M + H_2O$$
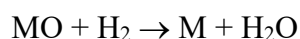
As a result, the thermal conductivity of the gas flow reduces which is measured by a thermal conductivity detector (TCD). It is easier for the detector to record a clear signal by using gases with significant different in thermal conductivities. Typically, argon or nitrogen the preferred carrier gases. Moreover, to maintain a high detector sensitivity, the concentration of hydrogen in the mixture should be limited in the 1-10% range. This is due to the fact that the change of thermal conductivity is only proportional to mole fraction at low concentration of reactant gas in the mixture.

It is worth noting that TPR is not limited to the reduction of oxides. The study of coke deposits on catalysts can also be studied by TPR [48].

$$Coke + H_2 \rightarrow Hydrocarbons + H_2O$$

TPR results are greatly influenced by the programmed heating rate, hydrogen concentration in the flowing gas mixture and the flow rate of the gas flow. The experimental conditions should be wisely chosen to ensure good resolution of multistep reductions, and to obtain reliable data. The criteria were suggested to be followed: $S^o/(V \times C^o) = 55\text{-}140$ (s), and $\beta \times S^o/(V \times C^o) < 20$. In the equations β is the heating rate (^{o}C/s), S^o is the initial amount of reducible species in the sample (μmol), while V is the total flow rate of reducing gas (cm^3/s) and C^o is the initial concentration of the reducing gas (μmol/cm^3) [49].

2.4.5. Temperature Programmed Desorption (TPD)

Temperature programmed desorption (TPD) measures the desorption rate of adsorbed molecules as a function of temperature [50]. The obtained data can be interpreted to define and characterize active sites in adsorption and catalytic reactions. It can also be used in the study of adsorption states, binding energies, surface concentration and desorption kinetics.

TPD of CO_2 is a common method to measure the basicity of heterogeneous catalysts. The number and strength of basic sites can be calculated based on desorption profiles. The desorption temperature defines the basic strength while the peak area determines the amount of basic sites. Nevertheless, a definite scale and quantitatively exact numbers of sites was difficult to acquire. Hence, a relative comparison was recommended by carrying out the experiments under the same conditions for different catalysts [51].

In a typical TPD experiment, the sample is pre-treated in an appropriate way (in vacuum or in a flow of desired gas at desired temperature), depending on the measured material and the purpose of the experiment. The sample is then exposed to the adsorbate gas at a suitable temperature. The physiosorbed gas is subsequently removed from the sample by evacuation or by inert gas flow. The residual chemisorbed adsorbate is desorbed by heating the sample, where the temperature is gradually ramped up. The detector signal is proportional to the concentration of desorbed species from the surface [50]. The data obtained from the measurement is presented in a relationship between the variation of TCD signal and temperature (or time).

2.4.6. Gas chromatography (GC)

Gas chromatography (GC) is the most widely used method for separation and analysis of volatile compounds. GC technique is simple, fast, and applicable for many organic and inorganic materials, especially petrochemicals. According to the IUPAC, chromatography is a physical method of separation in which the components to be separated are distributed between two phases, one of which is stationary (stationary phase) while the other (mobile phase) moves in a definite direction [52]. Elution chromatography is a procedure in which the mobile phase is continuously passed through or along the chromatographic bed, while the sample is fed into the system as a finite slug.

Particularly, the sample is vaporized and carried by the mobile gas phase (carrier gas) through the column. Samples partition (adsorb) into the stationary liquid phase, based on their solubilities at the given temperature. The components of the sample (analyte) separate from one another based on their relative vapor pressures and affinities for the stationary bed. Apparently, the use of a gas for the mobile phase requires that the system be contained and leak-free, and this is usually accomplished with a glass or metal tube considered as the column. As the analytes leave the column when passing through the detector, the output signal is recorded as a chromatogram.

To quantify the analytes in a sample, chromatogram data is analyzed, peak area is integrated, or peak height is measured, and calculations are performed in desired units. With the developed electronic integrators and computers, peak area is a preferable measurement. There are five methods of quantitative analysis, namely area normalization, area normalization with response factors, external standard, internal standard and standard addition [52]. Among those methods, external standard (ESTD) is the most common approach for gas analyses.

Calibration sample and unknown samples are analyzed under the same condition. Calibration table with peak identification, retention time and window are stored in data system. In ESTD procedure, the response factor (RF) for each component is obtained from calibration since the detection sensitivity varies significantly between components. Response factors are normally considered as a

single point calibration curve. In subsequent sample analyses, the analyte's amount or concentration can be calculated based on response factor by eq. 2.7 below or interpolating from the calibration curve.

Amount or Concentration of component i = $RF_i \times$ the measured response (area or height of peak i)

$$RF_i = \frac{\text{the known amount (or concentration)}}{\text{the measured response (area or height) of the known amount}} \qquad (2.7)$$

3. EXPERIMENTAL

3.1. Materials and Equipment

All chemicals were used as received without any further purification. The details of the used chemicals and gases are summarized in Table 3.1.

Table 3.1. Details of used chemicals and gases

No	Materials	Chemical Formula	Manufacturer	Molecular Weight (g/mol)	Purity
1	Nickel (II) Nitrate Hexahydrate	$Ni(NO_3)_2 \cdot 6H_2O$	EMSURE	290.81	$\geq 99\%$
2	Iron (III) Nitrate Nonahydrate	$Fe(NO_3)_3 \cdot 9H_2O$	EMSURE	403.95	$\geq 99\%$
3	Magnesium Nitrate Hexahydrate	$Mg(NO_3)_2 \cdot 6H_2O$	EMSURE	256.41	$\geq 99\%$
4	Aluminum Nitrate Nonahydrate	$Al(NO_3)_3 \cdot 9H_2O$	EMSURE	375.13	$\geq 98.5\%$
5	Sodium Hydroxide	$NaOH$	AnalaR NORMAPUR	40.00	$\geq 99.2\%$
6	Sodium Carbonate	Na_2CO_3	EMSURE	105.99	$\geq 99.9\%$
8	Nitric acid	HNO_3	AnalaR NORMAPUR		$\geq 65\%$
9	Aluminum oxide, α-phase	$Al2O_3$	Sigma-Aldrich	99	$\geq 99\%$
10	Methane	CH_4	Yara Praxair	16	99.999%
11	Carbon dioxide	CO_2	Yara Praxair	44	99.999%
12	Helium	He	Yara Praxair	2	99.999%
13	Hydrogen	H_2	Yara Praxair	2	99.999%
14	Nitrogen	N_2	Yara Praxair	28	99.999%
15	Synthetic air	N_2, O_2	Yara Praxair	28.9	99.999%

3.2. Catalyst synthesis

In this study, catalysts were synthesized by two different methods. The precursors containing nickel, iron, magnesium, and aluminum ions are denoted as NiFe-x, where x represents the molar ratio of Fe and Ni in the reduced catalysts. The mass of Ni was kept constant at 20 wt.% in reduced catalysts.

The atomic ratio between divalent ions and trivalent ions $\left(n_{Mg^{2+}} + n_{Ni^{2+}}\right)\big/\left(n_{Al^{3+}} + n_{Fe^{3+}}\right)$ were kept constant at three. The compositions of the prepared catalysts are summarized in Table 3.2, where the denotations of the catalysts are also presented.

Table 3.2. Denotations and compositions of the prepared catalysts

Denotation	Fe/Ni molar ratio	Nominal catalyst compositions (wt.%)	Preparation method
NiFe-0	0	20 Ni – 0 Fe – 52 MgO – 28 Al$_2$O$_3$	Conventional
NiFe-0.1	0.1	20 Ni – 2 Fe – 52 MgO – 26 Al$_2$O$_3$	Conventional
NiFe-0.1-F	0.1	20 Ni – 2 Fe – 52 MgO – 26 Al$_2$O$_3$	Fast without aging step
NiFe-0.1-FA	0.1	20 Ni – 2 Fe – 52 MgO – 26 Al$_2$O$_3$	Fast with aging step
NiFe-0.2	0.2	20 Ni – 4 Fe – 52 MgO – 24 Al$_2$O$_3$	Conventional
NiFe-0.5	0.5	20 Ni – 10 Fe – 52 MgO – 19 Al$_2$O$_3$	Conventional
NiFe-1	1	20 Ni – 19 Fe – 51 MgO – 10 Al$_2$O$_3$	Conventional

3.2.1. Coprecipitation by conventional method

The HT-like catalysts were prepared by coprecipitation method at low supersaturation which was modified from Bhattacharyya *et al.* [34]. A stoichiometric amount of Mg(NO$_3$)$_2$.6H$_2$O, Al(NO$_3$)$_3$.9H$_2$O, Ni(NO$_3$)$_2$.6H$_2$O, and Fe(NO$_3$)$_3$.9H$_2$O were dissolved in 400 mL deionized water to form a cation solution with total ion concentration of 0.5 M. NaOH and Na$_2$CO$_3$ with a sufficient amount were dissolved in 400 mL deionized water in a 1-liter flask as anion solution. The nitrate solution was added dropwise by a graduated funnel to the basic solution under vigorous stirring at room temperature in 2 hours (1-2 drops/second). When the addition is completed, the suspension was adjusted to pH 10 with concentrated nitric acid and stabilized at ambient temperature for 30 minutes. The slurry was subsequently aged at 85 °C under continuous nitrogen purge and vigorous stirring for 18 hours. After filtering under vacuum condition, the solids were washed several times with deionized water until pH of the filtrate was neutral. The filter cake is finally dried at 90 °C overnight, crushed and sieved (< 250 µm).

The as-prepared catalysts were calcined using quartz reactor with flowing synthetic air at 600 ºC for 6 hours. The temperature was increased to 600 ºC at a ramp rate of 5 ºC/min.

3.2.2. Coprecipitation by fast injection method

The Fe/Ni molar ratio $x = 0.1$ was chosen for the two samples prepared by fast injection method at high supersaturation. The fast synthesis procedure of HT-like material was based on Tathod an Gazit's work [35] with modification. 100-mL of metal nitrate solution with a total metal concentration of 0.25 M was used. The 500-mL base solution containing a sufficient amount of NaOH and Na_2CO_3 (pH $\approx$ 13) was prepared. The nitrate solution was added rapidly using syringe into the base solution under vigorous stirring. Upon the complete addition, the mixture was stirred for 1 minute. The mixture was centrifuged at 10,000 rpm for 10 minutes. The supernatant liquid was decanted, and the solid residue was washed several times with deionized water. The gel-like mass was obtained after washing was dried at 90 ^{o}C overnight, crushed and sieved (< 250 μm). The catalyst is denoted as NiFe-0.1-F.

To study the effect of aging for this synthesis method, the same procedure was followed. However, when the addition is completed, the mixture was further aged at 85 ^{o}C under continuous nitrogen purge and vigorous stirring for 18 hours. After centrifugation, the obtained solid was centrifuged, washed, dried, crushed and sieved with similar conditions as mentioned above. The as-prepared sample was denoted as NiFe-0.1-FA.

The as-prepared catalyst precursors were calcined at the same conditions as the catalyst prepared by the fast method.

3.2.3. Reduction and passivation

The calcined catalysts were reduced under 50 vol% H_2/N_2 with a flow rate of 100 mL/min in a fixed-bed tubular reactor at 600 ^{o}C for 4 hours. The temperature was also ramped up to 600 ^{o}C at 5 ^{o}C/min. For another experiment, the catalysts were reduced at 800 ^{o}C for 2 hours.

After reduction, the samples were cooled down to room temperature in flowing nitrogen. The passivation was conducted for 2 hours at room temperature using a mixture of 4 vol% of synthetic air and 96 vol% of nitrogen, and a flow rate of 100 mL/min.

3.3. Catalyst Characterization

3.3.1. X-ray diffraction (XRD)

X-ray diffraction study of the catalysts (as-prepared, calcined, reduced and spent samples) were performed by Bruker-AXS Microdiffractometer D8 Advance using CuKα radiation source. The patterns were recorded with 2θ range of 10-90°, with a step interval of 1°/min.

3.3.2. Nitrogen adsorption-desorption

The nitrogen adsorption-desorption experiments were conducted with the Micromeritics Tristar 3000 instrument at -196 $^{\circ}$C using liquid nitrogen. Before the analysis, the samples were degassed at 180 $^{\circ}$C overnight under vacuum condition.

3.3.3. Hydrogen chemisorption

Micromeritics ASAP 2020 Plus instrument was used to carry out hydrogen chemisorption analysis. Calcined samples (200 mg) were degassed in helium flow at 200 $^{\circ}$C (ramp rate of 5 $^{\circ}$C/min) for 2 hours, reduced in flowing hydrogen at 600 $^{\circ}$C for 4 hours (ramp rate of 5 $^{\circ}$C/min), and cooled down in flowing nitrogen. Finally, volumetric hydrogen chemisorption was performed at 35 $^{\circ}$C. The stoichiometry factor was one hydrogen atom per nickel atom [53].

3.3.4. Temperature programmed reduction (TPR)

H_2-TPR measurements were performed on a Micromeritics Autochem II ASAP 2920 analyzer equipped with a thermal conductivity detector (TCD). Calcined samples (~80 mg) were degassed at 200 $^{\circ}$C in He flow for 20 minutes to remove adsorbed CO_2 and H_2O. After cooling to 50 $^{\circ}$C, the reducing gas mixture (10 vol% H_2 in argon) at a flowrate of 50 mL/min was purged to the samples. The temperature was ramped to 950 $^{\circ}$C at 10 $^{\circ}$C/min and kept for 30 minutes.

3.3.5. Temperature programmed desorption (TPD)

The same equipment Micromeritics Autochem II ASAP 2920 was subsequently used to measure CO_2-TPD results after H_2-TPR analysis. The reduced samples were degassed at 600 $^{\circ}$C in helium (He) for 30 minutes and then cooled to 80 $^{\circ}$C. A flow of 6 vol% CO_2 in argon (50 mL/min) was then introduced for 1 hour. Weakly adsorbed CO_2 was desorbed by He flow for 1 hour. The CO_2-TPD were recorded by heating up the samples to 800 $^{\circ}$C under He flow (50 mL/min) at a heating rate of 10 $^{\circ}$C/min. The data was smoothed and deconvoluted into Gaussian distribution by Origin Lab software.

3.4. Catalytic activity tests

A schematic of the experimental setup is illustrated in Fig. 3.1. The gas feed units consisting of N_2, H_2, CH_4 and CO_2 were controlled and monitored by mass-flow controllers (Alicat). Each gas line had a manual pressure regulation valve set at 5 bar. A pressure gauge was also installed to indicate the pressure of the reactor. The reactor is a fixed-bed tubular reactor made from high-temperature resistance metal alloy with internal diameter of 11.81 mm, heated by an electrical oven controlled by

a temperature regulator (Eurotherm 3280). The thermocouple (type K) was installed inside the reactor and positioned on the top of the catalyst bed. The gasses were preheated before entering the reactor by passing through a gas line in the oven. A pressure relief valve and a pressure gauge were also installed after the reactor.
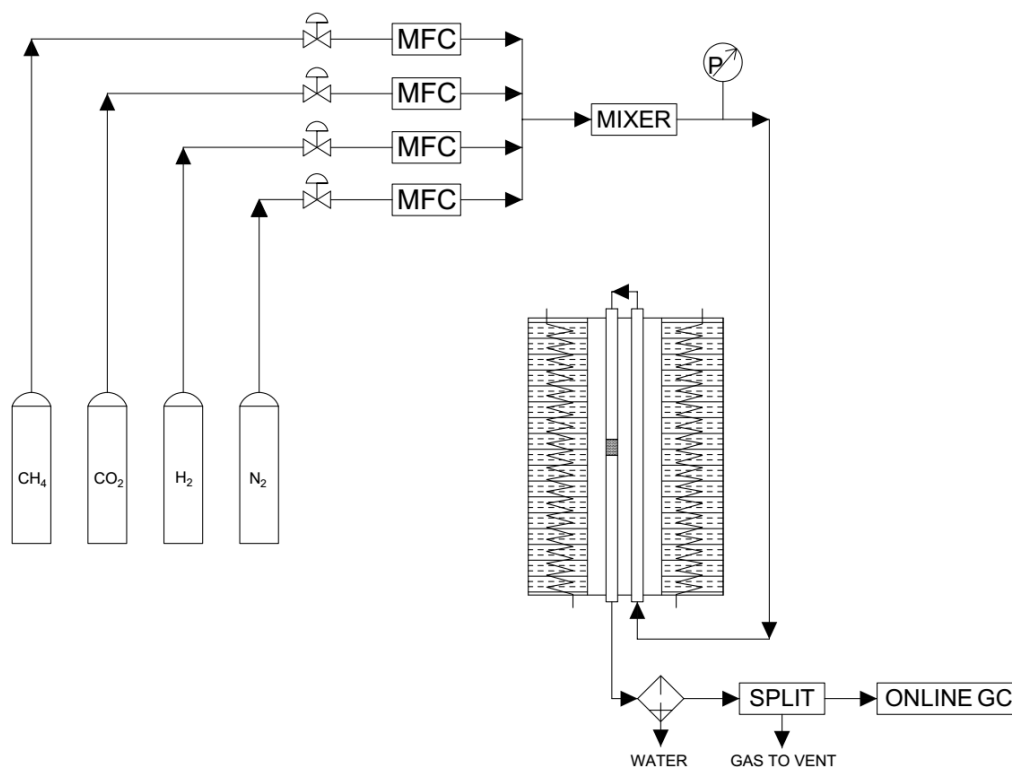

Figure. 3.1. Schematic representation of the experimental set-up for DRM activity test

In a typical experiment, 50 mg of calcined catalyst (< 250 µm) mixed with 500 mg of α-alumina (100-200 mesh) was used to avoid hot spots and blockage in the catalyst bed. A quartz plug was placed inside the reactor to keep the catalyst in position during reaction. The reduction was conducted at 600 ºC for 4 hours in a flow of 50 vol% H_2/N_2 (100 mL/min). Subsequently, only pure nitrogen was purged into the reactor and the reactor temperature was ramp up to the DRM reaction temperature of 700 ºC (heating rate of 5 ºC/min). The reactant gas was then introduced, which was a mixture of CH_4 and CO_2 (50:50 vol%) at 200 mL/min (240,000 mL/g^{-1}.h^{-1} of GHSV). The pressure of reaction was at 1 bar during the process.

The off-gas mixture passed through a coalescing filter to remove water before entering the gas chromatograph (Agilent 7890B) for online analysis. A stable input flow to the GC was ensured by a splitter. It splits the off-gas flow into two parts, one part for measurement and the other to ventilation. He and N_2 were used as the carrier gases. CH_4, CO_2, CO and H_2 were analyzed using a molecular sieve-packed column with two TCD detectors.

The reactant conversion was calculated by eq. 3.1-3.3, where n_i^{in} and n_i^{out} are the number of moles of each gas in the reactor inlet and outlet.

$$X_{CH_4} = \frac{n_{CH_4}^{in} - n_{CH_4}^{out}}{n_{CH_4}^{in}} \times 100\% \qquad (3.1)$$

$$X_{CO_2} = \frac{n_{CO_2}^{in} - n_{CO_2}^{out}}{n_{CO_2}^{in}} \times 100\% \qquad (3.2)$$

$$H_2/CO = \frac{n_{H_2}}{n_{CO}} \qquad (3.3)$$

4. RESULTS AND DISCUSSIONS

4.1. Characterization of catalysts

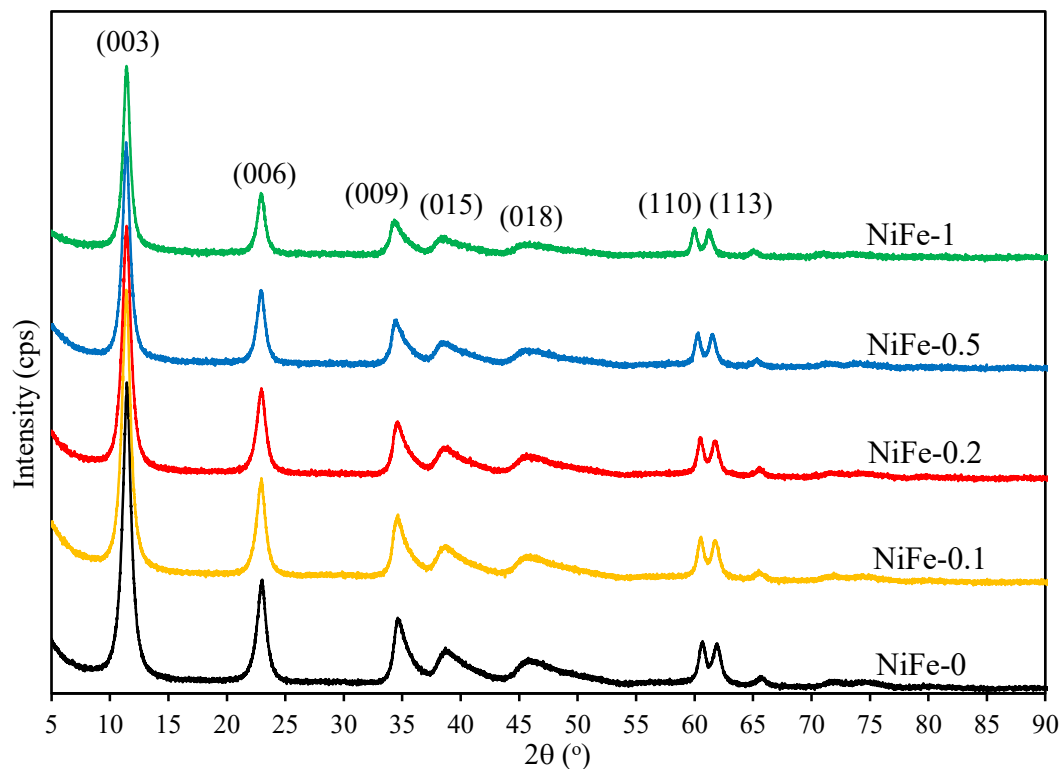### 4.1.1. XRD of as-prepared catalysts

Figure 4.1. XRD patterns of as-prepared catalysts synthesized by conventional method

XRD patterns of the as-prepared catalysts synthesized by conventional precipitation method exhibits characteristic diffraction peaks of magnesium aluminum hydroxide carbonate HT (JCPDS 22-0700), as shown in Fig. 4.1. NiFe-0 HT precursors have sharp and symmetrical peaks at 2θ of 11.45°, 23.0°, 60.7° and 61.9°, attributed to (003), (006), (110), and (113) planes of HT; while the other broad peaks at 2θ of 34.6°, 38.7° and 45.8° are assigned to (009), (015) and (018) planes, respectively. From the diffractograms it can be seen that no impurities were formed during the synthesis for precursors with different Fe/Ni ratios [54].

The thickness of one layer constituting a brucite-like sheet and one interlayer [9] was calculated based on the d-spacing of the (003) reflection. The calculated values are summarized in Table 4.1. The layer thickness was in a close range of 0.772 - 0.776 nm, which increased slightly with increasing Fe content, and was slightly smaller than 0.784 nm for $Mg_6Al_2(OH)_{16}CO_3.4H_2O$. Moreover, the average cation-cation distance in the brucite-like layer [9, 28], which is also half of the lattice parameter a, was calculated from $d(110)$ spacing (Table 4.1). For the sample NiFe-0, $d(110)$ was smaller than 0.1540 mm of $Mg_6Al_2(OH)_{16}CO_3.4H_2O$. It could be due to the substitution of smaller Ni^{2+} ion to

larger Mg^{2+} ion in the lattice (radii of 0.069 nm for Ni^{2+} and 0.072 for Mg^{2+}). As the Fe content increased in the sample, the distance between two metal ions increased. It is reasonable since Fe^{3+} cations have slightly larger radii than Al^{3+} (0.055 nm for Fe^{3+} and 0.054 nm for Al^{3+}). These results were in good agreement with Li *et al.* who showed that the unit cell length *a* depends on the nature of the cations (iconic radius) following Vegard's law [27], while the thickness of the layers only depends on the anion layer (M^{2+}/M^{3+} ratio) [28].

Table 4.1. d-spacing of the (003) and (110) refection plane

Catalysts	2θ (°)	d(003) (nm)	2θ (°)	d(110) (nm)
$Mg_6Al_2(OH)_{16}CO_3.4H_2O$	11.28	0.784	59.98	0.1540
NiFe-0	11.45	0.772	60.65	0.1526
NiFe-0.1	11.42	0.774	60.53	0.1528
NiFe-0.2	11.42	0.774	60.51	0.1529
NiFe-0.5	11.40	0.776	60.26	0.1535
NiFe-1	11.40	0.776	60.00	0.1541

XRD patterns of the as-prepared precursors synthesized by fast injection method with high supersaturation are presented in Fig. 4.2. The diffractograms again indicate that HT-like structure without impurities were formed for both of the samples with and without aging step. Similar characteristic peaks are observed which position at the same angle, resulting in similar lattice parameter and metal ions distance compared to the NiFe-0.1 precursor synthesized by the conventional method. Therefore, it can be confirmed that pure HT precursors with high crystallinity were obtained by both conventional and fast injection method. Ni^{2+} and Fe^{3+} successfully incorporated into the HT structure. All cations were expected to highly disperse and homogeneously distribute in the brucite-like layers.
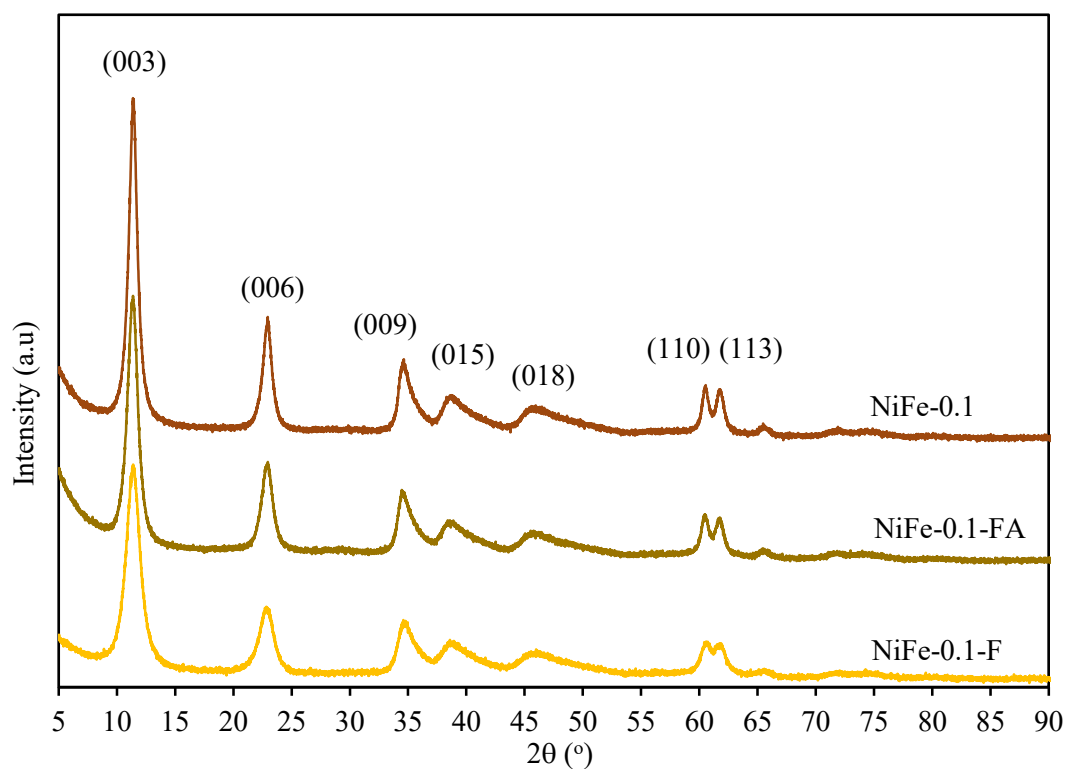
Figure 4.2. XRD patterns of the as-prepared NiFe-0.1 precursors
by fast injection and conventional method
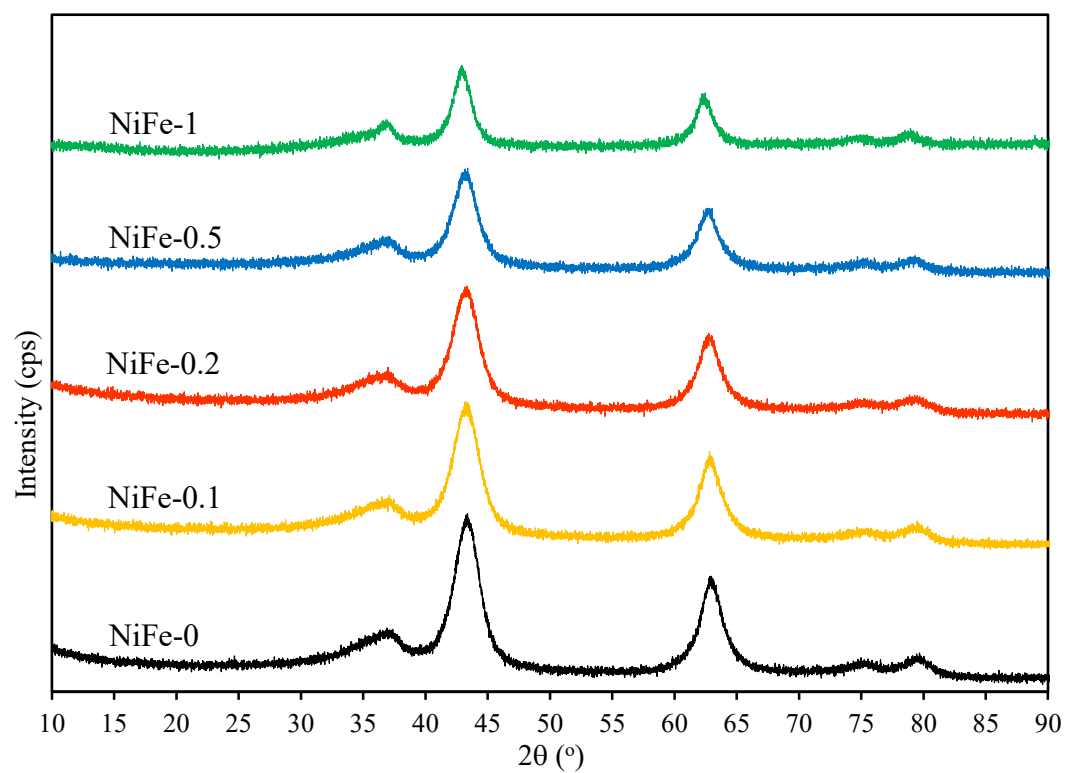
4.1.2. XRD of calcined catalysts

Figure 4.3. XRD patterns of calcined catalysts synthesized by conventional method

After calcination at 600 °C for 6 hours, the decomposition of HT-like precursors was considered to be completed since only the diffraction peaks of mixed oxides are observed in XRD diffractograms, as presented in Fig. 4.3. The XRD patterns show similar peaks in all calcined samples, except that the peak intensity decreases when Fe content increases. The oxide crystallite sizes calculated by Scherrer equation show that all samples had small particles size (4-5 nm), demonstrating the advantage of catalyst synthesis via HT precursors.

The peaks of calcined samples are attributed to diffraction of NiO (JCDPS 01-089-5881) at 2θ of 37.0°, 43.3°, 62.7°, 75.2°, 79.4°, but could also be overlapped with $MgAl_2O_4$, $NiFe_2O_4$, $NiAl_2O_4$, and Fe_2O_3. Mette *et al.* reported that at moderate calcination temperature (350 °C and 600 °C), only rock-salt-type phase (NiO or MgO) was observed for NiMgAl oxides derived from HT. When the calcination temperature is increased to 800 °C and higher, crystalline spinel phase was detected. However, due to the similar diffraction patterns of spinels and mixed oxides, no detailed phase identification could be revealed by XRD analysis. The temperature of 600 °C was chosen as appropriate calcination condition for HT-like materials because no segregation of individual species would occur [55].

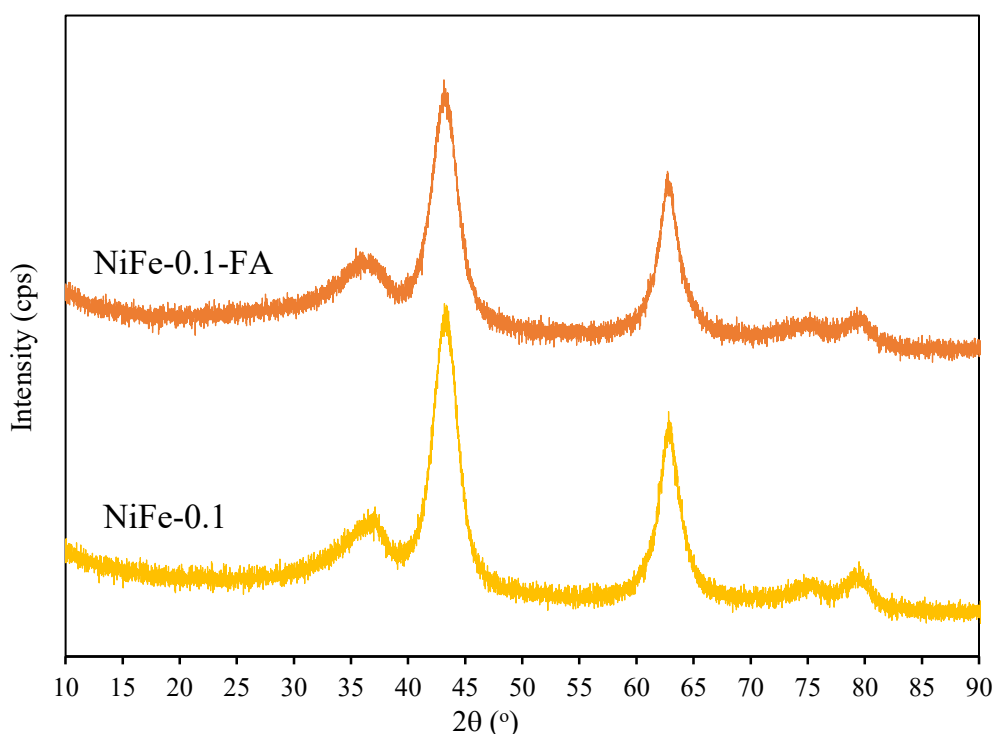Figure 4.4. XRD patterns of calcined catalysts synthesized by fast injection and conventional method

The catalyst synthesized by fast injection method with aging step was calcined, denoted as NiFe-0.1-FA. XRD pattern of this sample shows indifferent diffraction peaks compared to sample NiFe-0.1, as displayed in Fig. 4.4. The oxide particles of samples prepared by two different methods were also found similar in crystallite size.

4.1.3. XRD of reduced-passivated catalysts

All samples synthesized by conventional method was reduced at 600 °C for 4 hours and further passivated in diluted air. The reduced-passivated samples were also analyzed measured by XRD as shown in Fig. 4.5. The characteristic peak of metallic Ni [JCDPS 03-065-2865] at 2θ of 51.8° is observed for all catalysts, attributed to diffraction of the (200) plane. The peak shifted to lower angle (from 51.8° to 50.6°) upon increasing Fe content, indicating the formation of Ni-Fe alloy [27].
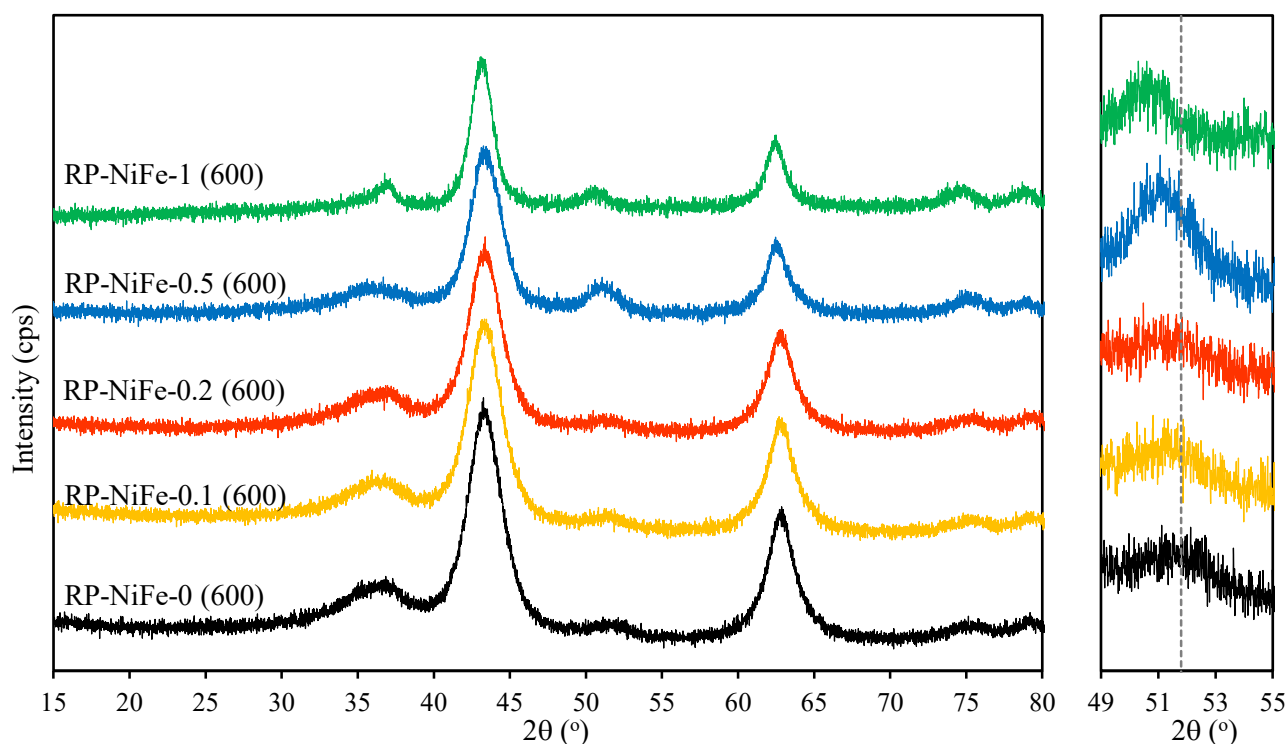
Figure 4.5. XRD patterns of reduced-passivated catalysts at 600 °C

The d(200) spacing of face-centered cubic (fcc) γ-Fe is 0.1823 nm, which is positioned at 2θ of 49.9°, while d(200) of fcc Ni was at 2θ of 51.8°. Hence, the d(200) spacing of Ni-Fe alloys varies between those of Ni and γ-Fe, should increase with increasing Fe content (i.e. smaller in angle). Fig. 4.6 describes the correlation between d(200) calculated from XRD data and Fe/Ni molar ratio, which agrees well with the results of Li *et al.* and Kim *et al.* [7, 27]. On the other hand, the overlapped peaks of NiO, $NiAl_2O_4$, $NiFe_2O_4$, $MgAl_2O_4$ at 2θ of 37°, 43.4°, 62.9° are still depicted with high intensity, which could be due to the incomplete reduction at the temperature of 600 °C.
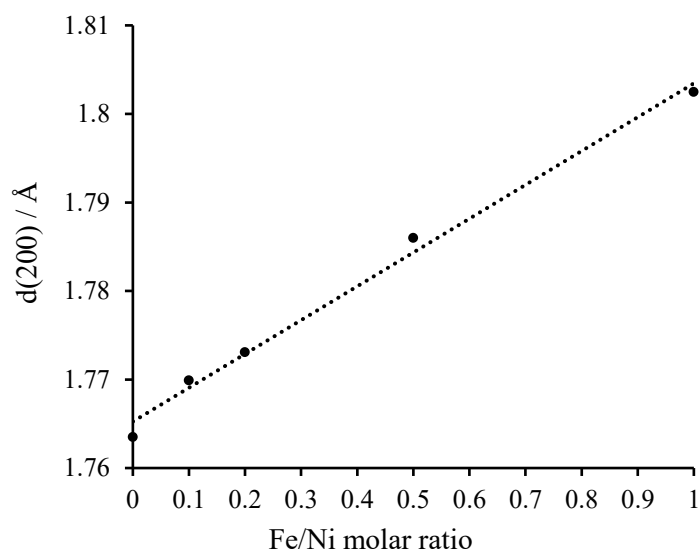
Figure 4.6. Correlation between the *d*(200) spacing and Fe/Ni molar ratio

Consequently, a higher reduction temperature was tested on selected samples to study the effect of reduction temperature on the structure of catalysts. Three samples were reduced at 800 °C for 2 hours, and the XRD patterns of the resulting catalysts are presented in Fig. 4.7.
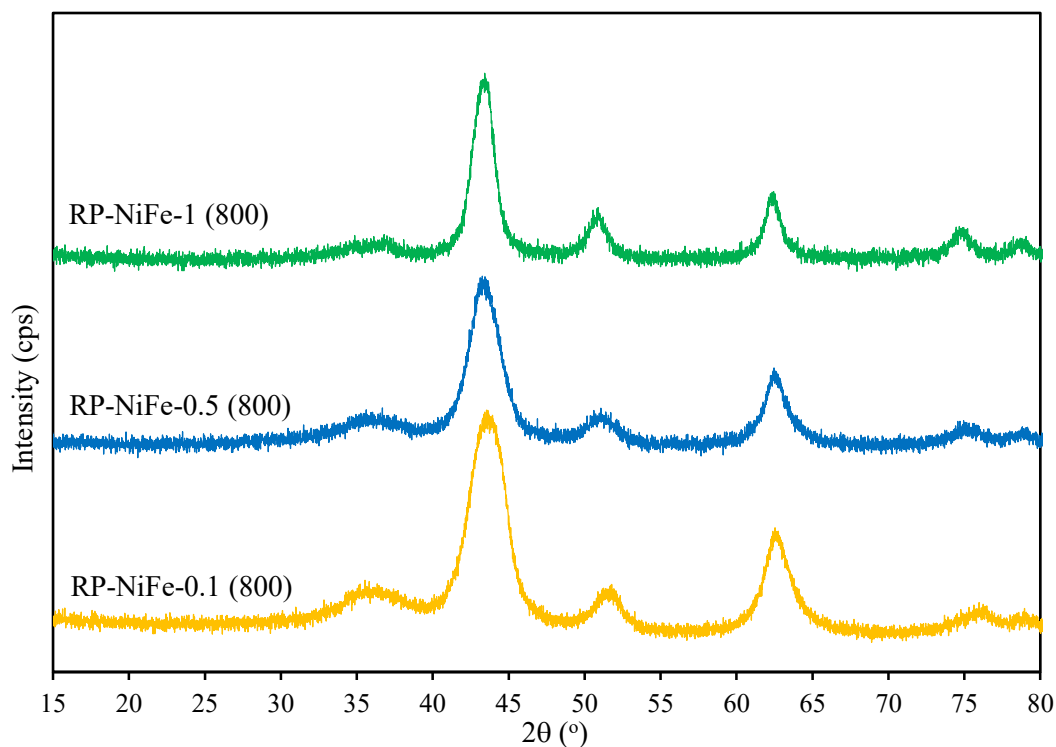
Figure 4.7. XRD patterns of reduced-passivated catalysts at 800 °C

The peaks attributed to metallic Ni are found to locate at the same angles compared to samples reduced at 600 °C (Fig. 4.5). The Ni peak intensities became stronger when the reduction temperature is increased. Presumably, the higher reduction temperature would increase the reduction degree of

the Ni as well as the Ni crystallite sizes. Nevertheless, the overlapped peaks can still be observed, which again can be explained by the incomplete reduction or unsuccessful passivation of the reduced samples.

4.1.4. Nitrogen adsorption-desorption
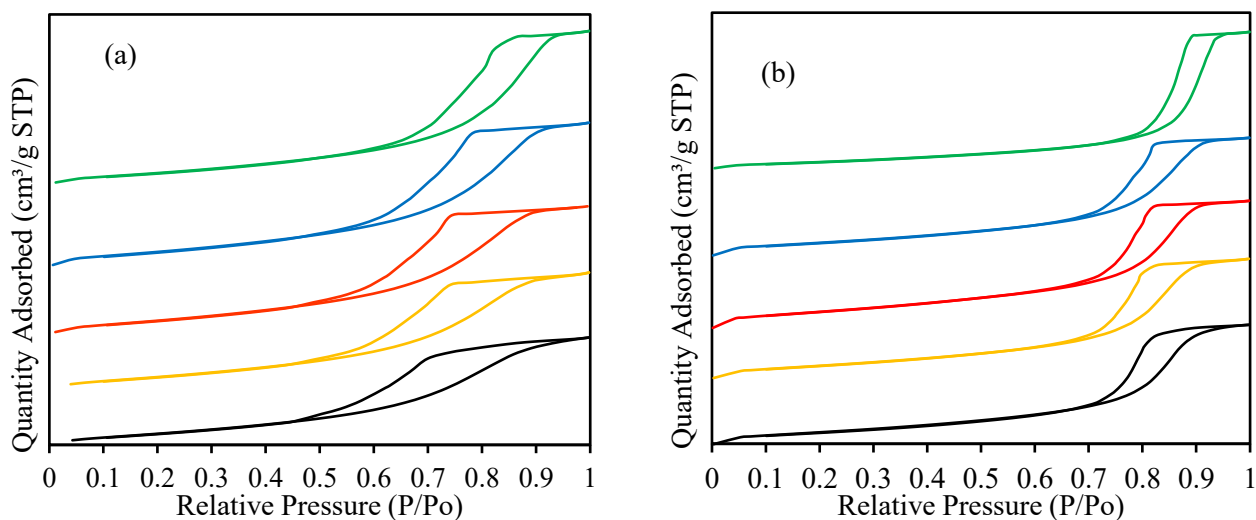
Figure 4.8. N_2 adsorption-desorption isotherms of as-prepared (a) and calcined (b) catalysts synthesized by conventional method NiFe-x. From bottom x = 0, 0.1, 0.2, 0.5 and 1
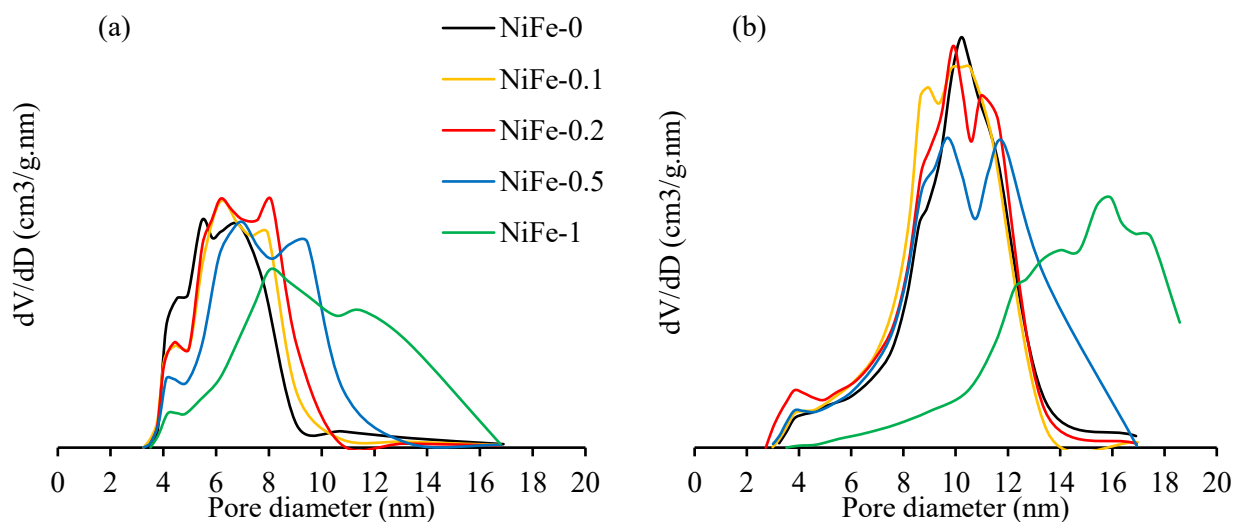
Figure 4.9. Pore size distribution of as-prepared (a) and calcined (b) catalysts synthesized by conventional method

The N_2 adsorption-desorption isotherms are shown in Fig 4.8 (a) and (b) for the as-prepared precursors and calcined catalysts. They represent typical type IV isotherms with hysteresis loop at high P/Po range, according to IUPAC classification. It is characteristic of mesoporous material, which can be further confirmed by the pore size distributions.

Fig. 4.9 (a) and (b) presents the pore size distributions for the as-prepared and calcined samples, respectively. The average pore size was 6-8 nm for the as-prepared precursors, while it was larger at 10-12 nm for calcined samples. One exception is NiFe-1 catalyst with the highest Fe content, has wider pore size distributions amongst others. The average pore sizes are between 8-12 nm and 12-16 nm for the as-prepared precursor and calcined catalyst, respectively.

The textural properties including specific surface area and pore volume are summarized in Table 4.2. Overall, the as-prepared HT-like precursors had high surface area and pore volume, which are consistent with reports by Kalai *et al.*, Duller *et al.* and Tang *et al.* [56-58]. BET specific surface area and BJH pore volume of the HT precursors increased upon increasing in Fe content, except for catalyst NiFe-0.5 and NiFe-1.

Table 4.2. Textual properties of as-prepared and calcined catalysts

Sample	BET Specific surface area (m^2/g)		BJH Pore volume (cm^3/g)	
	As-prepared	Calcined	As-prepared	Calcined
NiFe-0	132	205	0.33	0.59
NiFe-0.1	143	216	0.35	0.59
NiFe-0.2	152	247	0.38	0.62
NiFe-0.5	154	208	0.41	0.58
NiFe-1	136	141	0.42	0.65
NiFe-0.1-FA	225	246	0.44	0.61
NiFe-0.1-F	1.3	-	0.018	-

After calcination, the layer structure of initial HT was lost, and more pores and channels were opened, which led to the increase of surface area as well as pore volume in the calcined samples [59]. Theoretically, the precursors undergo a weight loss of 38% (calculated based on chemical formula). Experimentally, the precursors lost 42% in weight which can explained by physical loss and excessive moisture in the material before calcination. It is noticeable that with a small addition of Fe into the Ni-based precursor, the calcined catalysts had higher specific surface area as compared to monometallic Ni catalyst.

The textural properties of catalysts prepared by fast injection method are also summarized in Table 4.2. The aging step dramatically influenced the textural properties of the catalysts. The fast-method

catalyst with aging step (NiFe-0.1-FA) interestingly possessed the largest surface area as well as pore volume, both for the as-prepared and calcined samples. On the contrary, the sample NiFe-0.1-F without aging had the smallest surface area (only 1 m²/g) and pore volume (0.018 cm^3/g), indicating the advantage and importance of aging on the morphology of the catalyst. During aging, more HT layers were stacked together to form larger agglomerates with higher surface area and larger pore volume [35].

One of the striking differences between catalysts synthesized by fast injection method and conventional method with aging step is the uniform pore size of both fresh and calcined samples, as shown in Fig. 4.10. The pore size distributions of the catalyst NiFe-0.1-FA prepared by fast method were narrowed at 6.6 nm for fresh sample and at 8.4 nm for calcined sample, while a wider range of pore diameter was observed for NiFe-0.1 catalyst prepared by conventional method.
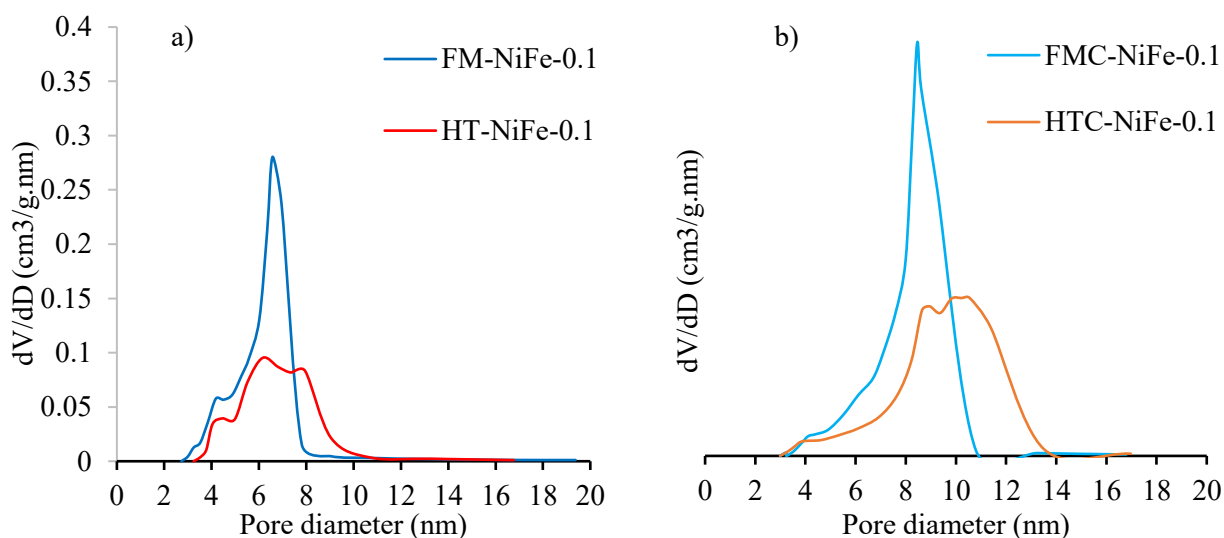
Figure 4.10. Pore size distribution of as-prepared (a) and calcined (b) catalysts synthesized by conventional and fast method

It can be explained that fast injection method with high supersaturation gives a higher rate of nucleation and a larger number of crystallization nuclei. During aging step, the nuclei agglomerate and form larger crystals with more regularity and perfection in shape and size. Tathod and Gazit reported that fast injection method promoted nucleation and restricted growth, consequently formed smaller particles with high uniformity. In contrast, neither the rate of nucleation nor crystal growth was dominant during coprecipitation at low supersaturation, which consequently resulted in larger particles with wider size distribution [35].

4.1.5. Hydrogen chemisorption

Chemisorption of H_2 on Fe is a complex and activated process [60-63]; hence, it is assumed that H_2 only chemisorbed on metallic Ni. As detailed in Table 4.3, the amount of H_2 consumed in chemisorption measurement decreased with the increase in Fe content in the reduced catalyst. Such decrease in the dispersion of Ni could be explained by the partial cover of Ni surface by Fe, or the formation of Ni-Fe alloy after reduction, both could prevent the chemisorption of H_2 on Ni. It is worth mentioning that the chemisorption capability sharply reduced when Fe/Ni molar ratio is over 0.1.

Table 4.3. H_2 chemisorption and TPR data of the catalysts prepared by conventional method

Catalyst	H_2 chemisorption (μmol/g)	Ni dispersion (%)	H_2 consumption (TPR) (μmol/g)	Nominal content (mmol/g$_{cat}$)		Reduction ratio $\dfrac{n_{H_2 \text{ consumed in TPR}}}{n_{Ni^{2+}} + n_{Fe^{3+}}}$
				Ni	Fe	
NiFe-0	79.22	4.65%	3.14	3.2	0.0	0.97
NiFe-0.1	68.33	4.01%	3.90	3.2	0.3	1.10
NiFe-0.2	38.63	2.27%	4.50	3.2	0.6	1.18
NiFe-0.5	4.06	0.24%	5.26	3.1	1.6	1.13
NiFe-1	3.86	0.23%	9.12	3.0	3.0	1.52

4.1.6. TPR

Reduction behavior of the calcined samples were investigated by TPR measurements. TPR profiles of the calcined catalysts are represented in Fig. 4.11. For the NiFe-0 catalyst, a single peak at 797 °C was observed, ascribed to the reduction of Ni^{2+} in strong interaction with the support. This result is in line with literature [27, 40, 64, 65] and previous work of Kalai *et al.* [56].

It has been reported that calcination condition, type of support and TPR measurement condition influenced the redox properties of the material, particularly for Ni-based catalysts [66]. Pure NiO had a single reduction peak at 398 °C, Ni/Al$_2$O$_3$ had a single peak at ~420 °C, while Ni^{2+} species in mixed oxide MgO-Al$_2$O$_3$ support was harder to be reduced at ~600 °C (peak α) and ~800 °C (peak β) [6]. It was proposed that weakly-interacting NiO-support reacted with H_2 first (peak α), then NiAl$_2$O$_4$ spinel was reduced at higher temperature. For Ni/MgAl$_2$O$_4$ catalyst, peak β was reported to be in a range at 700-800 °C, decreasing with the increase in Ni loading content. Debek *et al.* [40] reported that

NiMgAl HT-derived catalysts (20 wt.% of Ni, calcined at 550 °C) had reduction peak at 835 °C. For pure Fe_2O_3, two reduction peaks representing for the sequential reduction of $Fe^{3+} \rightarrow Fe^{2+}$ and $Fe^{2+} \rightarrow Fe$ were reported at ~370 °C and at ~560 °C [67].
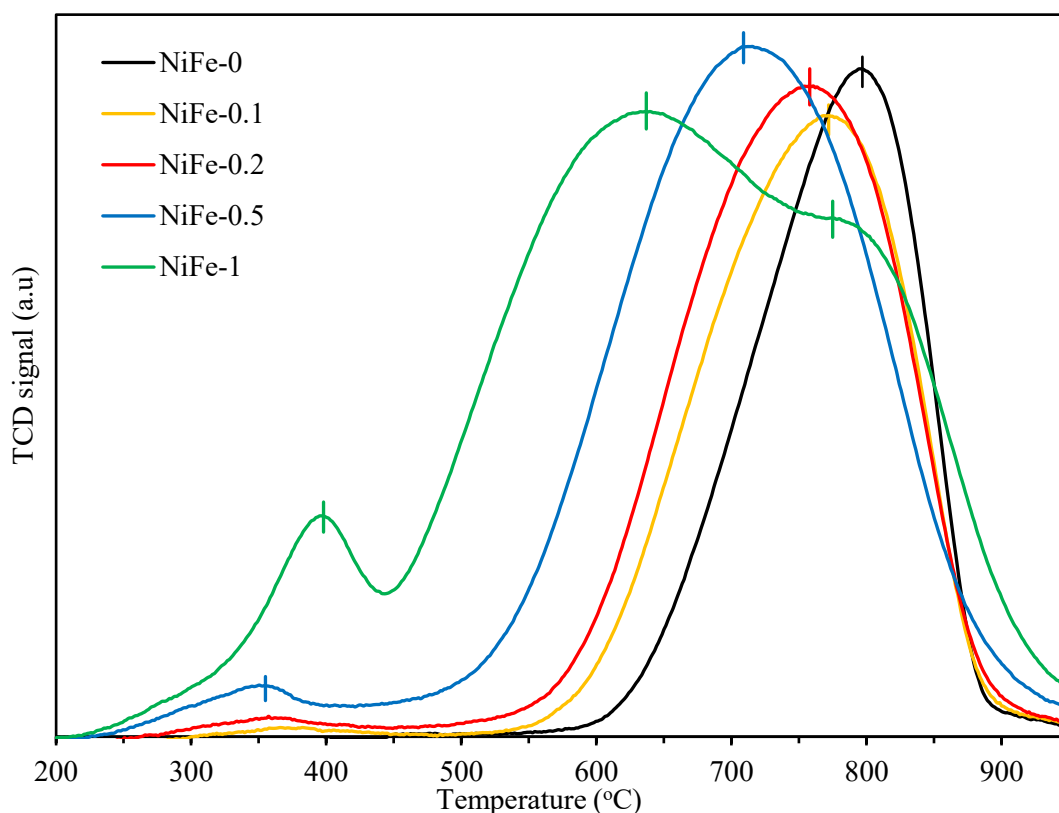

Figure 4.11. TPR patterns of calcined catalysts synthesized by conventional method

The reduction peaks for NiFe-0.1 and NiFe-0.2 were located at 772 °C and 758 °C, respectively. The reduction peaks shifted to lower temperatures compared to that of NiFe-0. Therefore, the presence of Fe has promoted the reduction of Ni. Moreover, a small broad peak at low temperature range (350-400 °C) could be assumed to the reduction of surface $Fe^{3+} \rightarrow Fe^{2+}$ [68].

In addition, the amount of H_2 consumption increased upon the increase of Fe content, as summarized in Table 4.3. The reduction ratio was determined as 0.97 mol_{H2}/mol_{Ni}, i.e. 97% reduction for monometallic catalyst. It implies that Ni might not be completely reduced. The increase in H_2 consumption could be accounted for the reduction of Fe species. The reduction ratio between total mol H_2 consumed and total mol of metals (last column of Table 4.3) was a comparative factor to define the role of secondary metallic Fe to the reducibility of Ni-based catalysts.

Nevertheless, the sequential reduction of Fe^{3+} species is only clearly demonstrated in the high Fe content sample. TPR profile of NiFe-1 shows three reduction peaks, one sharp peak located at 398 °C and two shoulder peaks at 637 °C and 775 °C. The first peak at 398 °C could be related to the reduction of $Fe^{3+} \rightarrow Fe^{2+}$, while it is complicated to determine specific reduction process of the last

two individual peaks due to the co-reduction of Ni and Fe species [69]. According to literature, TPR profile of $MgFeAl_2O_4$ spinel showed two peaks at 450-550 ^oC and 900-950 ^oC, which was explained by the sequential reduction of $Fe^{3+} \rightarrow Fe^{2+} \rightarrow Fe$ [68], whereas $NiFe_2O_4$ and $NiAl_2O_4$ were reduced at ~600 ^oC and ~800 ^oC, respectively [70].

In this case, the peak at 637 ^oC could be ascribed to the reduction of $NiFe_2O_4$, and the last peak at 775 ^oC could be due to the reduction of $NiAl_2O_4$. It is likely that different type of spinel could have been formed after the calcination of bimetallic Ni-Fe HT-derived catalysts.
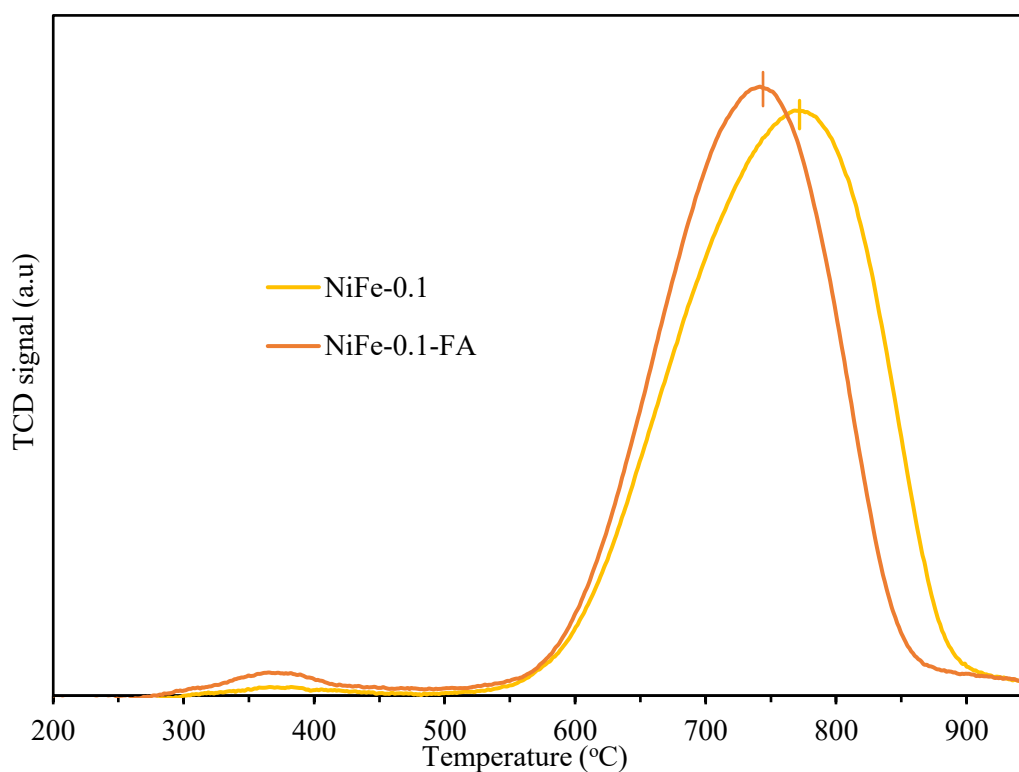
Figure 4.12. TPR profiles of NiFe-0.1 catalysts synthesized by conventional and fast method

Fig. 4.12 compares the TPR profile of the NiFe-0.1 and NiFe-0.1-FA catalysts. NiFe-0.1-FA was easier to be reduced by having a H_2-TPR reduction peak at lower temperature compared to NiFe-0.1 prepared by the conventional method. The consumption of H_2 in TPR measurement was also close at 3.71 μmol/g for NiFe-0.1-FA and 3.90 μmol/g for NiFe-0.1. The reduction peak of Fe^{3+} species was more visible for NiFe-0.1-FA than that of NiFe-0.1.

It is suggested that the uniformity in crystal growth enhanced the homogeneous distribution of metallic Ni and Fe in HT-like structure, resulted in a better dispersion on the surface and facilitated the reduction of both Ni and Fe species.

4.1.7. TPD

The basicity of the catalysts was analyzed by CO_2-TPD analysis after H_2-TPR analysis of the calcined samples. It was assumed that all samples had been reduced after TPR analysis. The CO_2-TPD profiles represented the basicity of reduced catalysts synthesized by both conventional and fast injection method, are displayed in Fig. 4.13 and Fig. 4.14.
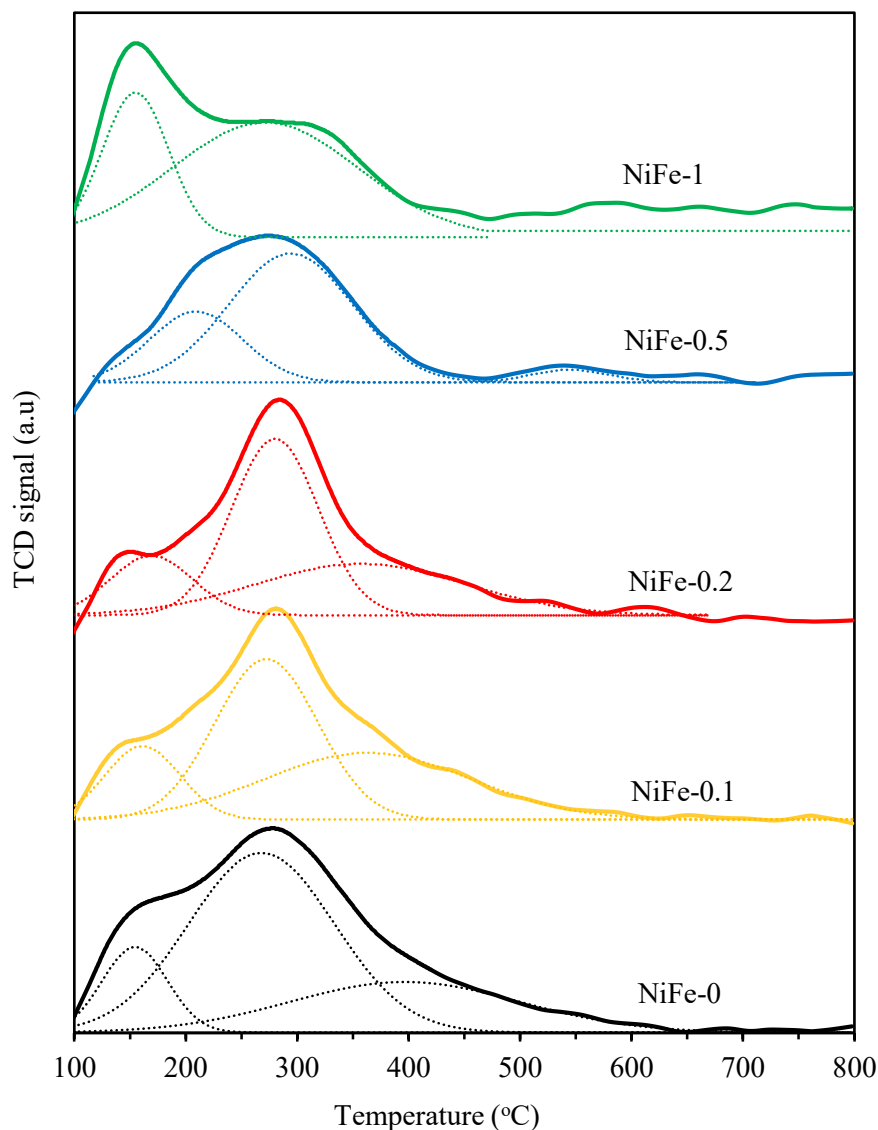
Figure 4.13. TPD profiles of reduced catalysts synthesized by conventional method

The total amount of CO_2 desorbed in the catalysts was calculated by the integration of the desorption profile. The total basicity ratio, as shown in Table 4.4, was calculated using the total mol of CO_2 desorbed from the NiFe-0 catalyst as reference. The ratios were all higher than unity, demonstrating that the basicity of bimetallic catalysts is stronger than monometallic catalyst. It could be explained that Fe^{3+} has Lewis basicity which increased the total basicity of the material [71]. However, the

increase in basicity was not proportional to the amount of Fe content. NiFe-0.5 was less basic than NiFe-0.1 and NiFe-1.
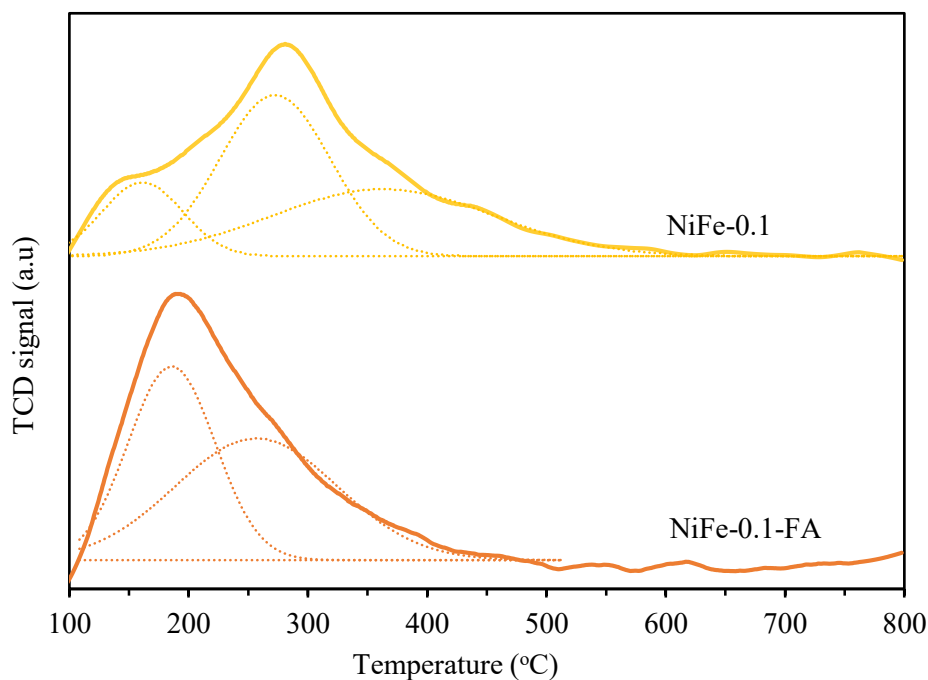
Figure 4.14. CO_2-TPD profiles of reduced catalysts synthesized by fast injection method

Interestingly, the NiFe-0.1-FA catalyst synthesized by fast injection method shows higher basicity than the NiFe-0.1 catalyst by conventional method. This result could be correlated to the effect of crystal nucleation and growth.

Table 4.4. Basicity distribution of the reduced catalysts

Sample	Weak sites (%)	Medium sites (%)	Strong sites (%)	Total basicity ratio (mol/mol)
NiFe-0	13%	61%	27%	Reference = 1
NiFe-0.1	15%	46%	38%	1.15
NiFe-0.2	15%	50%	35%	1.14
NiFe-0.5	28%	68%	4%	1.06
NiFe-1	32%	68%	0%	1.26
NiFe-0.1-FA	46%	54%	0%	1.22

Di Cosimo *et al.* [72] studied the infrared measurement and CO_2-TPD of Mg-Al HT and proposed three types of basic sites existing in the catalyst: weak Bronsted OH^- groups (bicarbonate), medium strength metal-oxygen Lewis pairs (bidentate carbonate) and strong Lewis basic sites - unsaturated

O^{2-} ions (unidentate carbonate), appearing at increasing decomposition temperature, as illustrated in Fig. 4.15. Based on the deconvolution into three Gaussian contributions corresponding to each type of basic sites, the distribution of basic sites of the catalyst was found to change upon the addition of Fe. According to Wu *et al.* and Carvalho *et al.* [71, 73], the first weak peak (~150 °C) was attributed to bicarbonates formed on OH⁻ groups on the surface, corresponding to weak basicity of these sites. The second peak at about 300 °C and the last peak at higher temperature (~425 °C) suggest the presence of medium and strong basic sites.
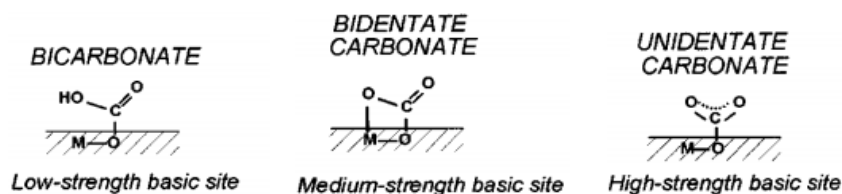

Figure 4.15. Adsorbed CO_2 species on basic solid [72]

For monometallic catalyst NiFe-0, the main contribution in basicity was medium sites (61%) and strong sites (27%). With the presence of Fe in the material, the strong basic sites increased to 38% for NiFe-0.1 and 35% for NiFe-0.2, respectively. However, when Fe/Ni molar ratio is higher than 0.2, there is a shift from strong sites to medium and weak sites, as can be seen in Table 4.4. Based on the DFT calculations of Kim *et al.* [7], this could be explained by the stronger Fe-O interaction compared to Ni-O interaction in the alloy, which favored the binding of oxygen-containing species, hence increased the medium-strength basic sites.

The NiFe-0.1-FA catalyst synthesized by fast injection method has basicity mainly constituted by medium-strength basic sites. The strong basic sites were not observed as in NiFe-0.1, suggesting that the majority of CO_2 adsorbed on the metallic surface by metal-oxygen bonds, not by the interaction with unsaturated O^{2-} ions from the $MgAl_2O_4$ mixed oxide support.

4.2. DRM activity

4.2.1. DRM activity of catalysts prepared by conventional method

DRM reactions were performed at 700 °C, 1 bar and gas flowrate of 200 mL/min ($CH_4:CO_2$ = 1:1), which corresponds to a GHSV of 240,000 $mL/g^{-1}.h^{-1}$. The CH_4 conversion, CO_2 conversion and H_2/CO ratio are presented in Fig. 4.16 – 4.18. For the monometallic NiFe-0 catalyst, the activity was stable for the first 3 hours then deactivation was observed. After 18 hours of time on stream (TOS), the conversion of CH_4 and CO_2 was 34.5% and 47.4%, respectively. Because of the RWGS reaction, the conversion of CO_2 is always higher than that of CH_4.
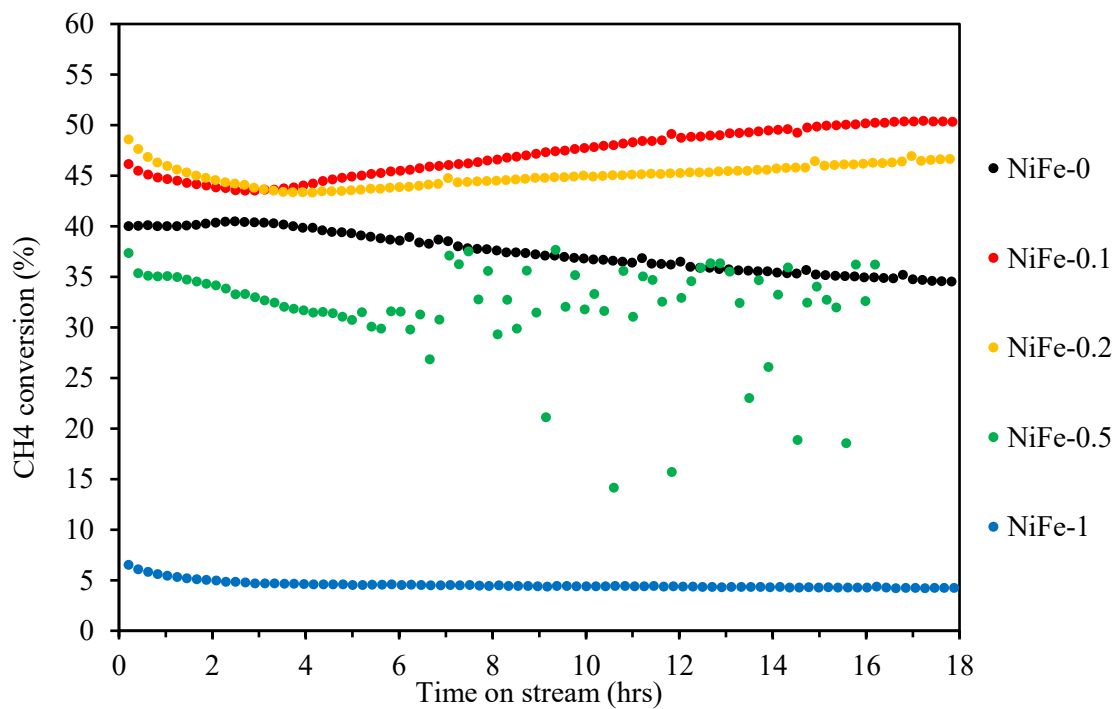
Figure 4.16. CH$_4$ conversions of catalysts synthesized by conventional method in DRM at 700 $^{\circ}$C
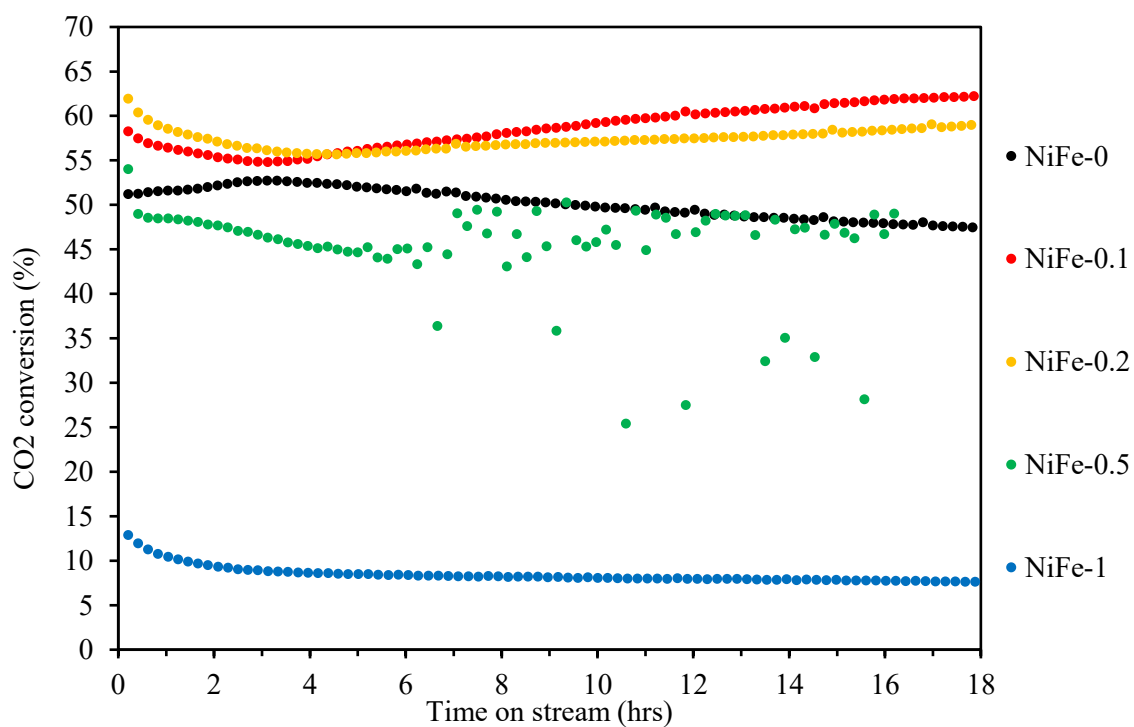

Figure 4.17. CO$_2$ conversions of catalysts synthesized by conventional method in DRM at 700 $^{\circ}$C
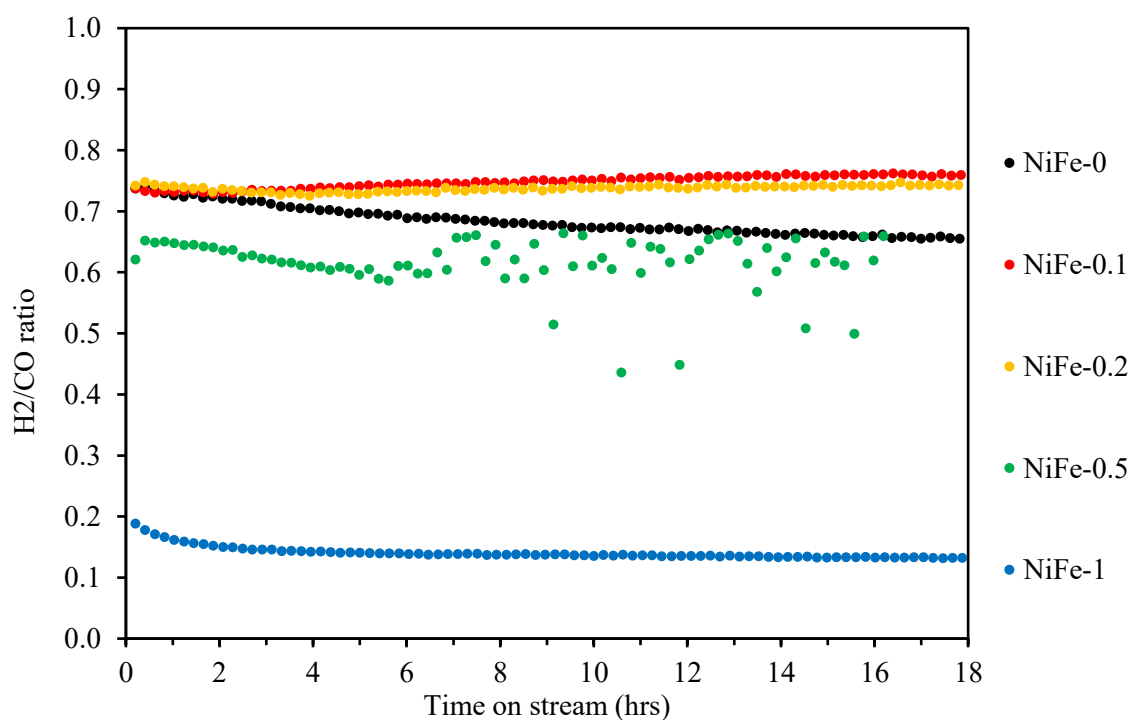
Figure 4.18. H_2/CO ratio of catalysts synthesized by conventional method in DRM at 700 °C

Interestingly, with a small addition of Fe (Fe/Ni of 0.1 and 0.2), the activity became higher, demonstrated by a higher conversion of both CH_4 and CO_2. Specifically, the NiFe-0.1 catalyst had the best catalytic activity. The initial conversion was higher than that of the NiFe-0 catalyst. The activity slightly decreased during the first 3 hours TOS, and then even gradually increased with 18 hours TOS. The final CH_4 and CO_2 conversion reached 50.3% and 62.2%, respectively. Catalyst with high Fe content, NiFe-0.5 and NiFe-1 had low activities. It might be due to a high coverage of Ni by Fe on the surface, or the formation of NiFe alloy, as demonstrated by H_2 chemisorption study.

Overall, H_2/CO ratio of all samples was lower than stoichiometric value of 1 due to RWGS reaction, as shown in Fig. 4.18. The same order of H_2/CO ratio as the activity of the catalysts was observed, with highest H_2/CO achieved by the NiFe-0.1 catalyst. The ratio steadily decreased during TOS, except that a stable ratio was maintained by NiFe-0.1 and NiFe-0.2 catalysts.

An abnormally oscillating performance had been observed for the NiFe-0.5 catalyst after 6 hours TOS, when the significant swing in catalytic activity was recorded. This phenomenon has been repeated for both runs, as shown in Fig. 4.19. Due to unstable catalytic activity, the H_2/CO ratio of catalyst NiFe-0.5 was also fluctuated. At this moment, no explanation can be given to clarify the abnormal behavior of the NiFe-0.5 catalyst.
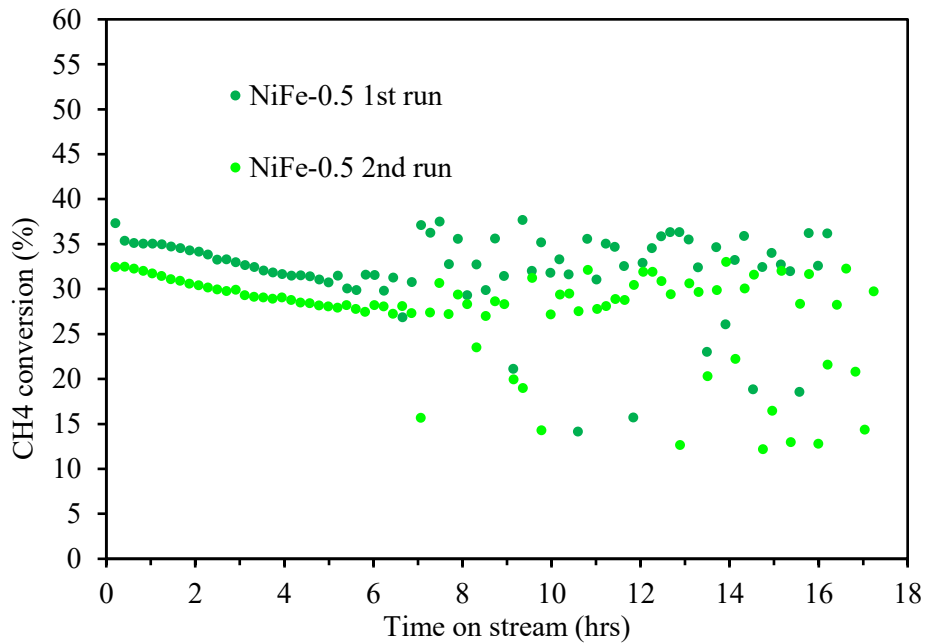
Figure 4.19. CH$_4$ conversion of two repeated DRM test the NiFe-0.5 catalyst

Li *et al*. investigated HT-derived Ni-Fe/Mg-Al bimetallic catalysts and proposed that the alloying of Ni with Fe improved the coke resistance of catalysts during steam reforming of tar produced from the pyrolysis of biomass. The yield of residual tar and coke deposited decreased upon increasing the Fe/Ni molar ratio [27]. The formation of Ni-Fe alloy during H$_2$ reduction and its decomposition during CO$_2$ oxidation are illustrated in Fig. 4.20 by Theofanidis *et al.* [8].
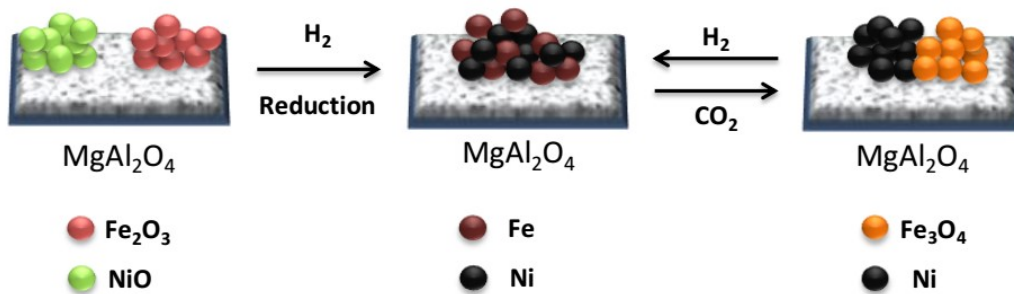
Figure 4.20. Schematic diagram of Ni-Fe alloy formation, during H$_2$-reduction, and decomposition, during CO$_2$ oxidation [8]

Kim *et al.* furthered proposed the mechanism of DRM reaction over Ni-Fe bimetallic catalysts, via Mars-van Krevelen mechanism [74], which are shown in the following reactions [7].

$$CH_4 \rightarrow 2H_2 + C$$

$$CO_2 + Fe \rightarrow CO + FeO$$

$$C + FeO \rightarrow CO + Fe$$

42
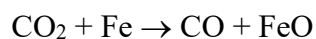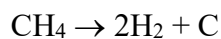
It was reported that during DRM reaction, Ni remained at metallic state Ni^0 and was deactivated by carbon deposition; while Fe in Ni-Fe alloys was partially oxidized to FeO by CO_2, segregated, and migrated at the surface, thus reacted with carbon deposits, and contributed to the suppression of carbon formation [7, 8].

In this study, different performance in the series of Ni-Fe bimetallic catalysts for DRM reaction were observed. Apparently, the content 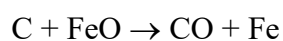of Fe influenced the structure and activity of the catalyst. Small addition of Fe was preferable with Fe/Ni molar ratio < 0.2. Hence, the small addition of Fe effectively enhanced the activity and stability while the high content of Fe in the alloy could lead to high coverage of Ni surface area or Ni-Fe alloy formation and reduced catalytic activity.

The NiFe-0.1 catalyst exhibited the largest increasing in activity for 18 hours TOS, it could be suggested that with an appropriate Fe addition, metallic Ni was almost free from coke deposition because of the positive role of Fe in carbon removal. Besides, the higher basicity, enhanced reducibility, smaller crystallite size and higher surface area could also have contributed to the superior catalytic behavior of the NiFe-0.1 catalyst.

4.2.2. The effect of reduction temperature on DRM activity

Figure 4.21. CH_4 and CO_2 conversion over NiFe-0.1 catalyst reduced at 600 °C (R600) and 800 °C (R800)

The effect of reduction temperature was studied using the NiFe-0.1 catalyst. Fig. 4.21 presents the CH_4 and CO_2 conversions over NiFe-0.1 catalyst reduced at 60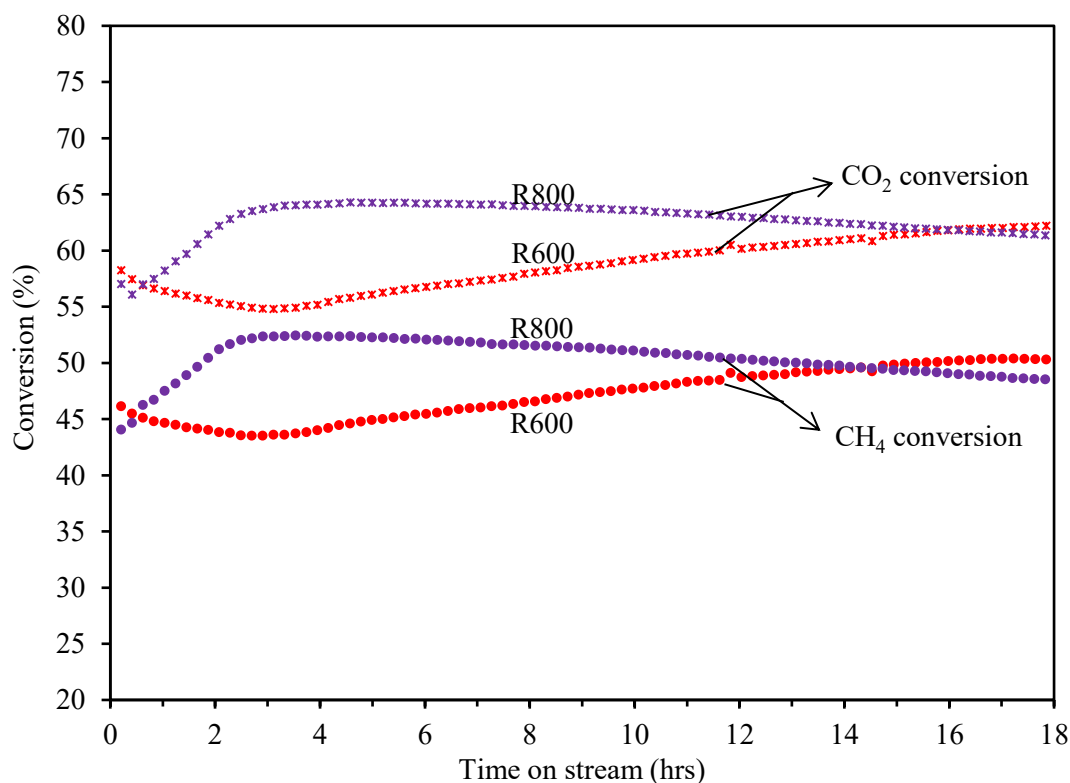0 °C and 800 °C. The catalyst reduced at 800 °C exhibited higher CH_4 and CO_2 conversion, which could be explained by a higher extent of reduction and a larger Ni surface area. The activity increased during the first 3 hours TOS, which is however followed by a steady decline. The final activity after 18 hours TOS was lower compared to the reduction at 600 °C.

Kim *et al*. and Margossian *et al*. also investigated the influence of reduction temperature on bimetallic Ni-Fe nano-catalysts supported on Mg(Al)O periclase for DRM [75]. The surface site was found to be impacted by reduction temperature. When the catalyst was reduced at 850 °C, more alloy presented on the surface compared to catalyst reduced at 650 °C. Under DRM reaction, the metal species evolved in a manner as illustrated in Fig. 4.22. Fe° tended to be partially oxidized to FeO located in the support, and FeO migrated into the support matrix to some extent. Larger quantity of coke was formed after reaction with a higher reduction temperature, indicating an ineffective Fe addition.

In this case, the higher activity of catalyst reduced at 800 °C in the first 3 hours TOS could be due to the increase in formation of Ni-Fe alloy which promoted the catalytic reaction. Subsequently, the decrease in activity and stability could be owing to the higher coke deposition.
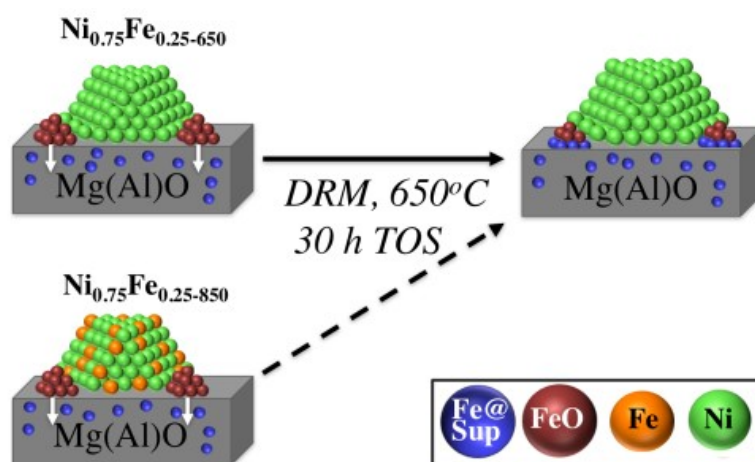
Figure 4.22. Scheme of the structure evolution during DRM at 650 °C for Ni-Fe nanoparticle catalysts reduced at different temperatures [75]

4.2.3. DRM catalytic activity of catalyst prepared by fast injection method

The NiFe-0.1-FA catalyst was tested under the same DRM condition as NiFe-0.1. The sample was pretreated with H_2/N_2 flow at 600 °C for 4 hours. The CH_4 and CO_2 conversions and H_2/CO ratio are shown in Fig. 4.23 and Fig. 4.24. The NiFe-0.1-FA demonstrated the best activity and stability amongst all prepared catalysts in this study. The highest CH_4 and CO_2 conversion was reached at

74% and 82% respectively, which was excellently stable during 18 hours TOS. As expected, H_2/CO ratio was 0.87, lower than 1 due to the RWGS reaction.
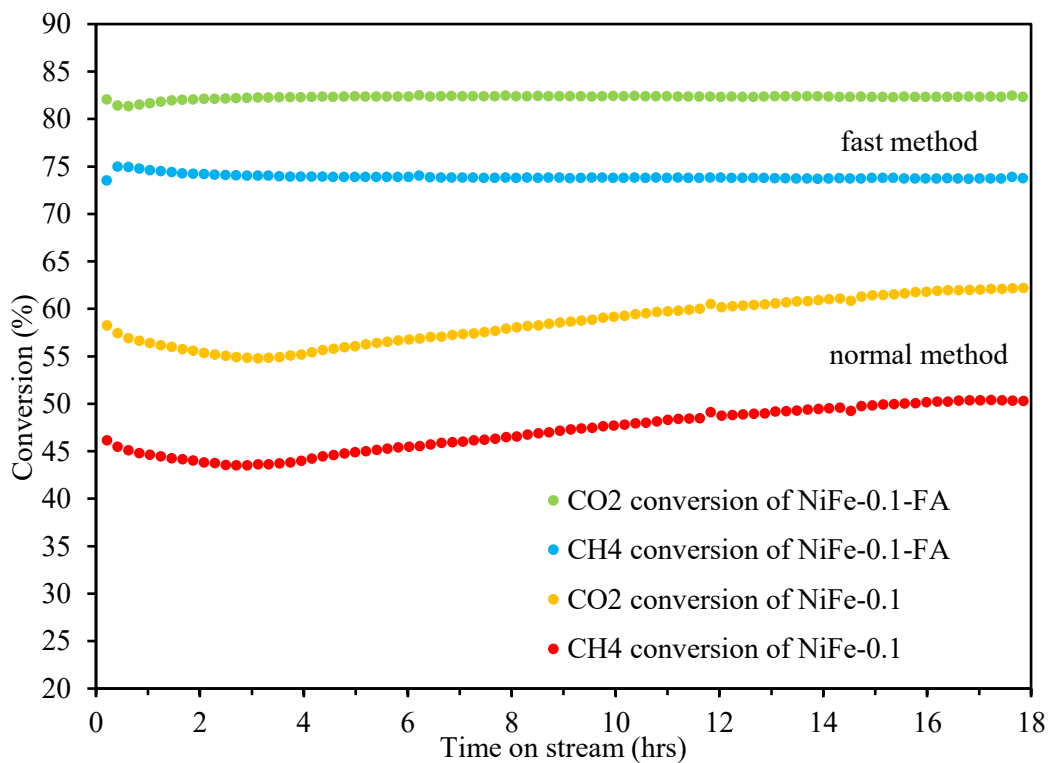
Figure 4.23. CH_4 and CO_2 conversions of the NiFe-0.1-FA and NiFe-0.1 catalysts in DRM at 700 ℃
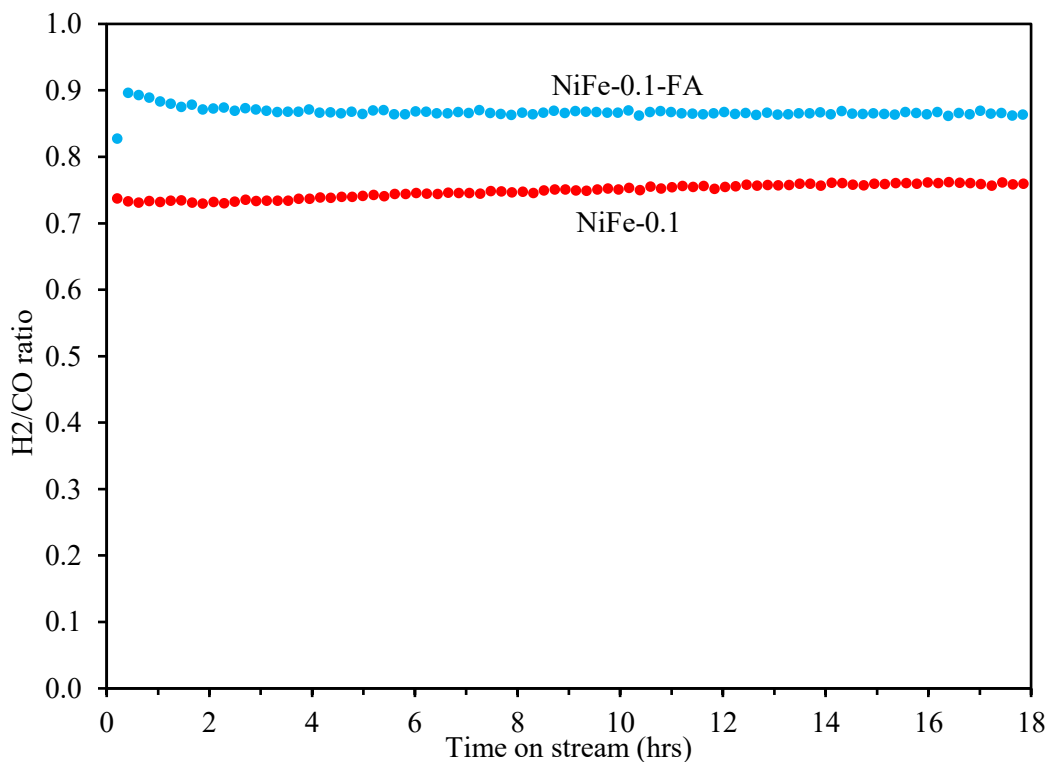
Figure 4.24. H_2/CO ratio of the NiFe-0.1-FA and NiFe-0.1 catalysts in DRM at 700 ℃

Ni particle size plays an important role in the resistance towards carbon formation as well as catalytic activity [76]. From a thermodynamic point of view, larger metal particles were more prone to coke deposition while highly dispersed small particles possessed better resistance to carbon formation [77]. This is consistent with experimental results by many researchers [16, 21, 78]. Recently, it has been reported by Kang *et al*. that Ni/silica catalyst (Ni/PS) synthesized using polyethyleneimine (PET) as ligands during a modified impregnation process, resulted in a narrower size distribution and better dispersion of metallic Ni compared to non-PET-added catalyst (Ni/S), as illustrated in Fig. 4.25. The smaller particles of the Ni/PS catalysts exhibited higher activity and stability towards DRM reaction at 750 °C during 40 hours TOS [79].
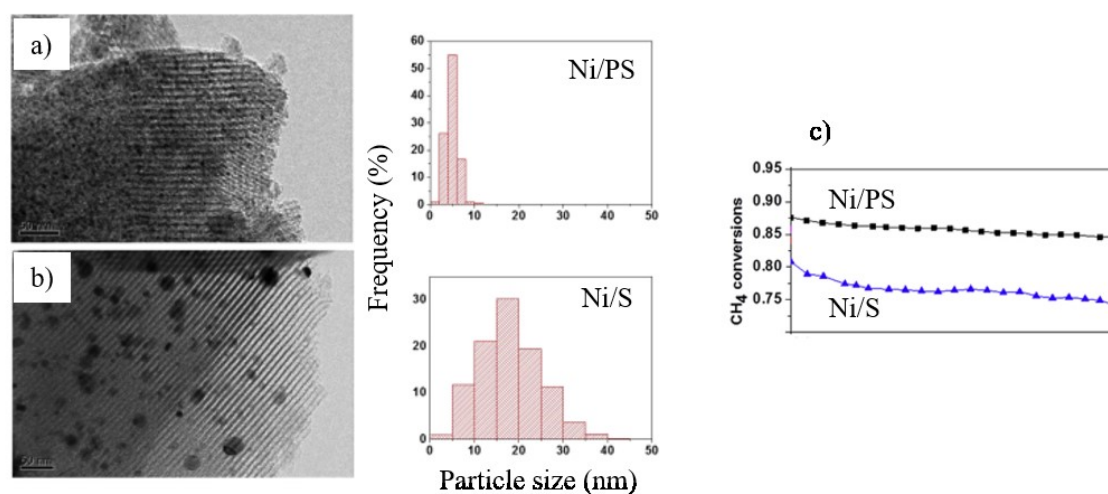
Figure 4.25. TEM images and particle size distribution histograms (a, b) and CH_4 conversion of catalyst Ni/PS and Ni/S in DRM reaction at 750 °C [79]

In this study, the superior in activity of the NiFe-0.1-FA catalyst could be explained by the small size and uniform distribution of the HT-like precursor, which further led to the small size and uniform dispersion of Ni-Fe alloy particles after calcination and reduction. Therefore, a higher activity and superior stability were achieved over this catalyst. Carbon formation was suppressed by not only the redox properties of Fe but also the enhanced dispersion of small Ni-Fe particles.

4.3. Characterization of spent catalysts

XRD patterns of the catalysts after DRM reaction are presented in Fig. 4.26. For the spent catalysts, graphite was found based on the strong peak at 2θ of 26° (JCPDS 41-1487). The diffraction peaks attributed to metallic Ni and Ni-Fe alloy are also observed at 2θ of 44.5° and 51.8°.

For Fe-rich catalyst (NiFe-0.5), catalyst reduced at 800 °C (NiFe-0.1 R800) and catalyst synthesized by fast injection method (NiFe-0.1-FA), more peaks at 2θ of 35.1°, 43.3°, 57.3°, 62.7° are ascribed to

Fe$_3$O$_4$ (FeO.Fe$_2$O$_3$), which also possibly overlapped with NiFe$_2$O$_4$. This observation is in line with the work of Abello *et al.* [69]. Moreover, these peaks were not depicted in the reduced-passivated samples (Fig. 4.5 and Fig. 4.7). Therefore, it could be assumed that Fe$_3$O$_4$ (FeO.Fe$_2$O$_3$) and/or spinel NiFe$_2$O$_4$ was formed during DRM reaction. It supports the proposed role of Fe in DRM that Fe was partially oxidized to form FeO and migrated on the surface of the catalysts, as illustrated in Fig. 4.22.

For the spent NiFe-0.1 and NiFe-0.2 catalysts, no such phase could be identified, which could be explained by the low content of Fe in the sample. The appearance of Fe$_3$O$_4$ (FeO.Fe$_2$O$_3$) and/or spinel NiFe$_2$O$_4$ for the spent NiFe-0.5 catalyst was due to high Fe content in the sample. However, the catalyst had poor activity because of high coverage of Fe on Ni surface. High reduction temperature could probably enhance the formation and segregation of iron oxide, which could explain the presence of FeO in the spent catalyst (NiFe-0.1 R800). Surprisingly, the spent NiFe-0.1-FA also presented Fe$_3$O$_4$ (FeO.Fe$_2$O$_3$) and/or spinel NiFe$_2$O$_4$ after DRM reaction. The fast injection method seems to have synthesized a material with very different structure compared to the conventional method. The existence of iron oxide and/or spinel could indicate the segregation of Fe from Ni from the structure after DMR. This could be one of the reasons for the superior activity of the NiFe-0.1-FA catalyst.
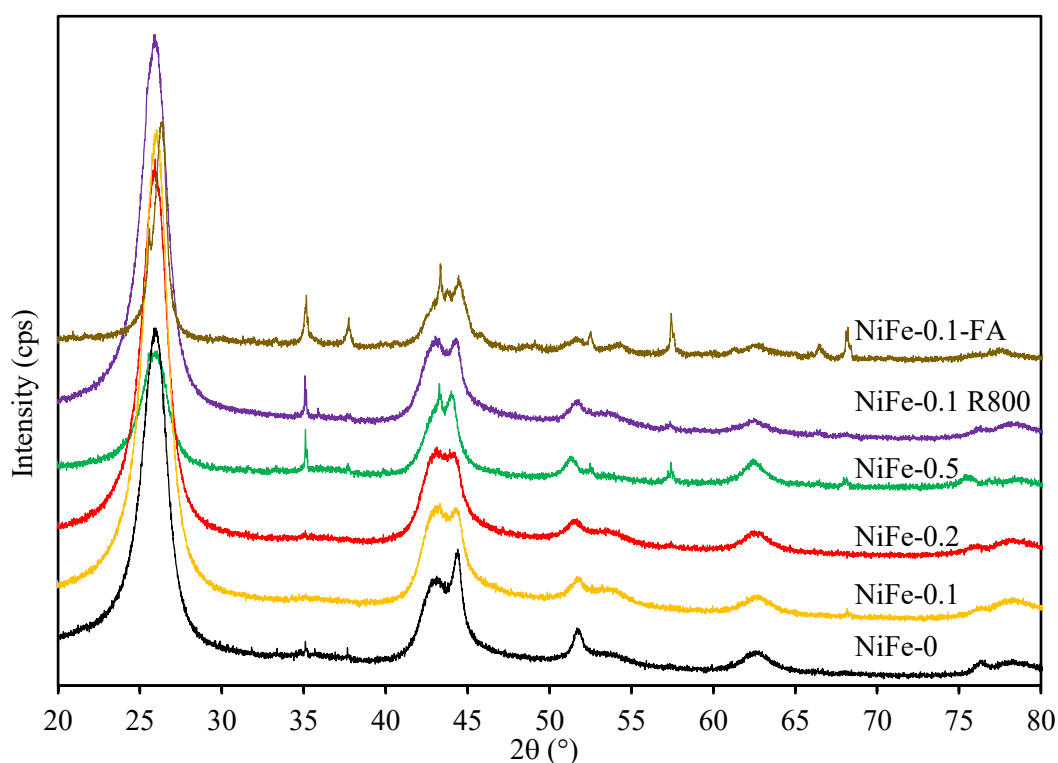
Figure 4.26. XRD of spent catalysts after 18 h DRM reaction at 700 °C

The crystallite sizes of Ni and/or Ni-Fe alloy particles after reaction was calculated based on the (200) diffraction plane at 2θ ~ 44.5° and are summarized in Table 4.5. In general, Ni-Fe alloy particles grew less in size compared to Ni particles in the monometallic NiFe-0 catalyst. As anticipated, the NiFe-

0.1-FA catalyst had the smallest crystallite size, from 3.7 nm after calcination to 7.1 nm after reaction. This could be explained by that not only smaller Ni particles are less susceptible to sintering [78] but also high-porosity supports have a low sintering rate [15].

Table 4.5. Crystallite size of oxides before reaction and metal particles of the spent catalysts after reaction

Sample	Crystallite size of oxide after calcination (nm)	Crystallite size of Ni and Ni-Fe alloy after reaction (nm)
NiFe-0	4.1	13.2
NiFe-0.1	3.8	9.2
NiFe-0.2	3.7	8.3
NiFe-0.5	4.1	9.7
NiFe-0.1-FA	3.7	7.1

5. CONCLUSIONS AND RECOMMENDATIONS

5.1. Conclusions

Bimetallic Ni-Fe supported on mixed oxides $MgAl_2O_4$ were successfully synthesized via HT precursors. Two coprecipitation methods were studied, namely conventional (low supersaturation) and fast injection method (high supersaturation). The Ni loading was kept constant at 20 wt.% while Fe content was varied with different Fe/Ni molar ratios (0, 0.1, 0.2, 0.5 and 1). Detailed characterization of catalysts by various methods demonstrated that:

- Ni^{2+} and Fe^{3+} were well incorporated into the HT-like structure by both synthetic methods. No impurities or segregation were observed based on XRD analysis.

- The as-prepared catalysts were completely decomposed after calcination at 600 ^{o}C for 6 hours. Mixed oxides and/or spinels were detected according to XRD analysis.

- Both as-prepared and calcined catalysts had high surface area and pore volume. The catalysts prepared by fast injection method without aging step presented significantly low surface area and pore volume, demonstrating the advantage of aging in catalyst synthesis.

- The benefit of fast injection method was shown by a narrower particle size distribution and higher surface area and pore volume compared with the conventional method.

- Ni-Fe alloy was formed after reduction at 600 ^{o}C for 4 hours with small crystallite size. Higher reduction temperature at 800 ^{o}C increased the crystallite size of the alloy.

- The increase in Fe content reduced the Ni metal surface area in the catalyst based on hydrogen chemisorption study.

- Lower reduction peaks of Ni species upon Fe addition indicates enhanced reducibility. The presence of Fe could have promoted the reduction of Ni.

- Stronger basicity was observed in bimetallic catalysts which could be explained by the Lewis basicity of Fe^{3+}, which increased the total basicity of the samples.

- In comparison with catalysts synthesized by conventional method, the catalyst synthesized by fast injection method was easier to be reduced, have higher basicity and particularly higher number of metal-oxygen sites.

The activity and stability of catalysts in DRM reaction were tested at 700 ^{o}C, 1 bar with high GHSV of 240,000 $mL/g^{-1}.h^{-1}$. The small addition of Fe into Ni-based catalysts (Fe/Ni molar ratio < 0.5) promoted catalytic activity towards DRM reaction compared to monometallic catalysts, while the addition of larger amount of Fe resulted in a poor activity. The optimal composition of Fe was found

at Fe/Ni molar ratio of 0.1. It was proposed that Fe particles in the alloy was partially oxidized and iron oxide reacted with deposit carbon located near the surface of metallic Ni. Hence, Fe could suppress carbon formation, maintain the surface area of active metallic Ni free of carbon and improve the activity and stability of the catalyst.

Higher reduction temperature at 800 ºC gives higher initial conversion, which could be due to higher reduction degree; however, high temperature gives lower stability, probably due to the formation of large particles which are more prone to carbon formation.

Interestingly, the catalyst synthesized by fast injection method presented the highest activity and the most stability amongst all prepared catalysts. Despite graphite was also found in the spent catalyst, deactivation was not observed during 18 hours TOS in DRM reaction. Since the catalytic performance of bimetallic catalysts are considerably influenced by the structure, surface composition and particle size, the preparation of uniform and well-dispersed alloy particles with an optimum composition is crucial for catalyst development. Therefore, coprecipitation at high supersaturation method could be a promising approach to synthesize highly active and stable bimetallic Ni-Fe HT derived catalyst.

5.2. Recommendations

More work can be done to further investigate on the advantage of the fast injection method. Although the catalysts synthesized by fast injection method presented superior activity, different Ni-Fe catalysts can be prepared to extensively study the influence of synthesis approach to the morphology and catalytic performance.

Advanced characterization can be carried out during DRM reaction in order to study the role of Fe in the bimetallic Ni-based catalysts. The analysis of spent catalyst is also crucial to determine the factors contributing to catalysts deactivation, e.g. carbon formation and/or metal sintering.

Moreover, it is practical to test the regenerability of the Ni-Fe catalysts towards oxidation-reduction treatment, which is one of the important factors for the commercialization of the catalysts.

REFERENCES

[1]   BP p.l.c, "BP Statistical Review of World Energy," 2018.

[2]   BP Energy Economics, "BP Energy Outlook 2018 Edition," 2018.

[3]   J.-M. Lavoie, "Review on dry reforming of methane, a potentially more environmentally-friendly approach to the increasing natural gas exploitation," (in English), *Frontiers in Chemistry,* Review vol. 2, no. 81, 2014.

[4]   R. Debek, M. Motak, T. Grzybek, M. Galvez, and P. Da Costa, "A Short Review on the Catalytic Activity of Hydrotalcite-Derived Materials for Dry Reforming of Methane," vol. 7, p. 32, 2017.

[5]   J. Xu, W. Zhou, Z. Li, J. Wang, and J. Ma, "Biogas reforming for hydrogen production over nickel and cobalt bimetallic catalysts," *International Journal of Hydrogen Energy,* vol. 34, no. 16, pp. 6646-6654, 2009.

[6]   J. Guo, H. Lou, H. Zhao, D. Chai, and X. Zheng, "Dry reforming of methane over nickel catalysts supported on magnesium aluminate spinels," *Applied Catalysis A: General,* vol. 273, no. 1, pp. 75-82, 2004.

[7]   S. M. Kim *et al.*, "Cooperativity and Dynamics Increase the Performance of NiFe Dry Reforming Catalysts," *Journal of the American Chemical Society,* vol. 139, no. 5, pp. 1937-1949, 2017.

[8]   S. A. Theofanidis, V. V. Galvita, H. Poelman, and G. B. Marin, "Enhanced Carbon-Resistant Dry Reforming Fe-Ni Catalyst: Role of Fe," *ACS Catalysis,* vol. 5, no. 5, pp. 3028-3039, 2015.

[9]   F. Cavani, F. Trifirò, and A. Vaccari, "Hydrotalcite-type anionic clays: Preparation, properties and applications," *Catalysis Today,* vol. 11, no. 2, pp. 173-301, 1991.

[10]   Y.-L. Du, X. Wu, Q. Cheng, Y.-L. Huang, and W. Huang, "Development of Ni-Based Catalysts Derived from Hydrotalcite-Like Compounds Precursors for Synthesis Gas Production via Methane or Ethanol Reforming," *Catalysts* vol. 7, no. 2, p. 70, 2017.

[11]   P. Cao, S. Adegbite, H. Zhao, E. Lester, and T. Wu, "Tuning dry reforming of methane for F-T syntheses: A thermodynamic approach," *Applied Energy,* 2017.

[12]   M. K. Nikoo and N. A. S. Amin, "Thermodynamic analysis of carbon dioxide reforming of methane in view of solid carbon formation," *Fuel Processing Technology,* vol. 92, no. 3, pp. 678-691, 2011.

[13]   K. Tomishige, D. Li, M. Tamura, and Y. Nakagawa, "Nickel-iron alloy catalysts for reforming of hydrocarbons: preparation, structure, and catalytic properties," *Catalysis Science & Technology,* vol. 7, no. 18, pp. 3952-3979, 2017.

[14] Y.-G. Chen, K. Tomishige, K. Yokoyama, and K. Fujimoto, "Catalytic Performance and Catalyst Structure of Nickel–Magnesia Catalysts for CO2 Reforming of Methane," *Journal of Catalysis,* vol. 184, no. 2, pp. 479-490, 1999.

[15] M. Argyle and C. Bartholomew, "Heterogeneous Catalyst Deactivation and Regeneration: A Review," *Catalysts,* vol. 5, no. 1, p. 145, 2015.

[16] D. Chen *et al.*, "Synthesis of carbon nanofibers: effects of Ni crystal size during methane decomposition," *Journal of Catalysis,* vol. 229, no. 1, pp. 82-96, 2005.

[17] V. Y. Bychkov, Y. P. Tyulenin, A. A. Firsova, E. A. Shafranovsky, A. Y. Gorenberg, and V. N. Korchak, "Carbonization of nickel catalysts and its effect on methane dry reforming," *Applied Catalysis A: General,* vol. 453, pp. 71-79, 2013.

[18] B. Abdullah, N. A. Abd Ghani, and D.-V. N. Vo, "Recent advances in dry reforming of methane over Ni-based catalysts," *Journal of Cleaner Production,* vol. 162, pp. 170-185, 2017.

[19] J.-E. Min, Y.-J. Lee, H.-G. Park, C. Zhang, and K.-W. Jun, "Carbon dioxide reforming of methane on Ni–MgO–Al2O3 catalysts prepared by sol–gel method: Effects of Mg/Al ratios," *Journal of Industrial and Engineering Chemistry,* vol. 26, pp. 375-383, 2015.

[20] K. Mette *et al.*, "High-Temperature Stable Ni Nanoparticles for the Dry Reforming of Methane," *ACS Catalysis,* vol. 6, no. 10, pp. 7238-7248, 2016.

[21] J.-H. Kim, D. J. Suh, T.-J. Park, and K.-L. Kim, "Effect of metal particle size on coking during CO2 reforming of CH4 over Ni–alumina aerogel catalysts," *Applied Catalysis A: General,* vol. 197, no. 2, pp. 191-200, 2000.

[22] C. Fan, Y.-A. Zhu, Y. Xu, Y. Zhou, X.-G. Zhou, and D. Chen, "Origin of synergistic effect over Ni-based bimetallic surfaces: A density functional theory study," *The Journal of Chemical Physics,* vol. 137, no. 1, p. 014703, 2012.

[23] Z. Bian, S. Das, M. H. Wai, P. Hongmanorom, and S. Kawi, "A Review on Bimetallic Nickel-Based Catalysts for CO2 Reforming of Methane," *ChemPhysChem,* vol. 18, no. 22, pp. 3117-3134, 2017.

[24] U.S. Geological Survey, "Mineral Commodity Summaries 2017," 2017.

[25] L. Wang *et al.*, "Catalytic performance and characterization of Ni-Fe catalysts for the steam reforming of tar from biomass pyrolysis to synthesis gas," *Applied Catalysis A: General,* vol. 392, no. 1, pp. 248-255, 2011.

[26] M. Koike, D. Li, Y. Nakagawa, and K. Tomishige, "A Highly Active and Coke-Resistant Steam Reforming Catalyst Comprising Uniform Nickel–Iron Alloy Nanoparticles," *ChemSusChem,* vol. 5, no. 12, pp. 2312-2314, 2012.

[27] D. Li, M. Koike, L. Wang, Y. Nakagawa, Y. Xu, and K. Tomishige, "Regenerability of Hydrotalcite-Derived Nickel–Iron Alloy Nanoparticles for Syngas Production from Biomass Tar," *ChemSusChem,* vol. 7, no. 2, pp. 510-522, 2014.

[28] V. Rives and M. a. Angeles Ulibarri, "Layered double hydroxides (LDH) intercalated with metal coordination compounds and oxometalates," *Coordination Chemistry Reviews,* vol. 181, no. 1, pp. 61-120, 1999.

[29] G. Fan, F. Li, D. G. Evans, and X. Duan, "Catalytic applications of layered double hydroxides: recent advances and perspectives," *Chemical Society Reviews,* 10.1039/C4CS00160E vol. 43, no. 20, pp. 7040-7066, 2014.

[30] Z. P. Xu, J. Zhang, M. O. Adebajo, H. Zhang, and C. Zhou, "Catalytic applications of layered double hydroxides and derivatives," *Applied Clay Science,* vol. 53, no. 2, pp. 139-150, 2011.

[31] D. R. Lide, *Handbook of Chemistry and Physics*. CRC Press, 1999.

[32] P. S. Braterman, Z. P. Xu, and F. Yarberry, "Layered Double Hydroxides (LDHs)," in *Handbook of Layered Materials*, S. M. Auerbach, K. A. Carrado, and P. K. Dutta, Eds.: USA, 2004.

[33] A. Dyer James, C. Scrivner Noel, and K. Dentel Steven, "A practical guide for determining the solubility of metal hydroxides and oxides in water," *Environmental Progress,* vol. 17, no. 1, pp. 1-8, 2006.

[34] A. Bhattacharyya, "Method of hydrocarbon reforming and catalyst precursor," United States Patent 6071433, 2000. Available: http://www.google.com.gi/patents/US6071433.

[35] A. P. Tathod and O. M. Gazit, "Fundamental Insights into the Nucleation and Growth of Mg–Al Layered Double Hydroxides Nanoparticles at Low Temperature," *Crystal Growth & Design,* vol. 16, no. 12, pp. 6709-6713, 2016.

[36] Z. P. Xu and G. Q. Lu, "Hydrothermal Synthesis of Layered Double Hydroxides (LDHs) from Mixed MgO and Al2O3: LDH Formation Mechanism," *Chemistry of Materials,* vol. 17, no. 5, pp. 1055-1062, 2005.

[37] R.-t. Wang, X.-p. Liang, Y. Peng, X.-w. Fan, and J.-x. Li, "Effect of the reaction temperature on nanocrystallites MgAl2O4 spinel ceramic precursor," *Journal of Ceramic Processing Research,* vol. 10, no. 6, pp. 780-782, 2009.

[38] J. Zhang, Y. F. Xu, G. Qian, Z. P. Xu, C. Chen, and Q. Liu, "Reinvestigation of Dehydration and Dehydroxylation of Hydrotalcite-like Compounds through Combined TG-DTA-MS Analyses," *The Journal of Physical Chemistry C,* vol. 114, no. 24, pp. 10768-10774, 2010.

[39] M. A. Ermakova, D. Y. Ermakov, G. G. Kuvshinov, and L. M. Plyasova, "New Nickel Catalysts for the Formation of Filamentous Carbon in the Reaction of Methane Decomposition," *Journal of Catalysis,* vol. 187, no. 1, pp. 77-84, 1999.

[40] R. Debek *et al.*, "Methane dry reforming over hydrotalcite-derived Ni-Mg-Al mixed oxides: the influence of Ni content on catalytic activity, selectivity and stability," *Catalysis Science & Technology,* vol. 6, no. 17, pp. 6705-6715, 2016.

[41] E. N. Kaufmann, *Characterization of Materials*. John Wiley & Sons, 2003.

[42] B. D. Cullity, *Elements of X-ray Diffraction*. Addison-Wesley Publishing Company Inc., 1956.

[43] U. Holzwarth and N. Gibson, "The Scherrer equation versus the 'Debye–Scherrer equation'," *Nature Nanotechnology,* vol. 6, p. 534, 2011.

[44] A. Chauhan and P. Chauhan, "Powder XRD Technique and its Applications in Science and Technology," *J. Anal. Bioanal. Tech.,* vol. 5, p. 212, 2014.

[45] S. Lowell, J. E. Shields, M. A. Thomas, and M. Thommes, *Characterization Of Porous Solids And Powders: Surface Area, Pore Size And Density*. Kluwer Academic Publishers, 2004.

[46] K. S. Sing *et al.*, "Reporting Physisorption Data for Gas/Solid Systems," in *Handbook of Heterogeneous Catalysis*, 2008.

[47] E. P. Barrett, L. G. Joyner, and P. P. Halenda, "The Determination of Pore Volume and Area Distributions in Porous Substances. I. Computations from Nitrogen Isotherms," *Journal of the American Chemical Society,* vol. 73, no. 1, pp. 373-380, 1951.

[48] "Chapter 11 Temperature programmed reduction and sulphiding," in *Studies in Surface Science and Catalysis*, vol. 79, J. A. Moulijn, P. W. N. M. van Leeuwen, and R. A. van Santen, Eds.: Elsevier, 1993, pp. 401-417.

[49] A. Gervasini, "Temperature Programmed Reduction/Oxidation (TPR/TPO) Methods," in *Calorimetry and Thermal Methods in Catalysis*, A. Auroux, Ed. UK, 2013.

[50] V. Rakic and L. Damjanovic, "Temperature Programmed Desorption (TPD) Methods," in *Calorimetry and Thermal Methods in Catalysis*, A. Auroux, Ed. UK, 2013.

[51] H. Hattori, "Heterogeneous Basic Catalysis," *Chemical Reviews,* vol. 95, no. 3, pp. 537-558, 1995.

[52] H. M. Mcnair and J. M. Miller, *Basic Gas Chromatography* USA: Wiley, 2009.

[53] C. H. Bartholomew, "Hydrogen adsorption on supported cobalt, iron, and nickel," *Catalysis Letters,* vol. 7, no. 1, pp. 27-51, 1990.

[54] M. del Arco, P. Malet, R. Trujillano, and V. Rives, "Synthesis and Characterization of Hydrotalcites Containing Ni(II) and Fe(III) and Their Calcination Products," *Chemistry of Materials,* vol. 11, no. 3, pp. 624-633, 1999.

[55] K. Mette *et al.*, "Stable Performance of Ni Catalysts in the Dry Reforming of Methane at High Temperatures for the Efficient Conversion of CO2 into Syngas," *ChemCatChem,* vol. 6, no. 1, pp. 100-104, 2014.

[56] D. Y. Kalai, K. Stangeland, Y. Jin, and Z. Yu, "Active and stable hydrotalcite derived Ni catalysts for CO2 reforming of methane: Comparison with catalysts by incipient wetness," *Journal of CO2 Utilization,* 2018.

[57] H. Dudder *et al.*, "The role of carbonaceous deposits in the activity and stability of Ni-based catalysts applied in the dry reforming of methane," *Catalysis Science & Technology,* vol. 4, no. 9, pp. 3317-3328, 2014.

[58] H. Tang, S. Li, D. Gong, Y. Guan, and Y. Liu, "Bimetallic Ni-Fe catalysts derived from layered double hydroxides for CO methanation from syngas," *Frontiers of Chemical Science and Engineering,* vol. 11, no. 4, pp. 613-623, 2017.

[59] M. Bellotto, B. Rebours, O. Clause, J. Lynch, D. Bazin, and E. Elkaïm, "A Reexamination of Hydrotalcite Crystal Chemistry," *The Journal of Physical Chemistry,* vol. 100, no. 20, pp. 8527-8534, 1996.

[60] Z. Yu, D. Chen, M. Rønning, T. Vrålstad, E. Ochoa-Fernández, and A. Holmen, "Large-scale synthesis of carbon nanofibers on Ni–Fe–Al hydrotalcite derived catalysts: I. Preparation and characterization of the Ni–Fe–Al hydrotalcites and their derived catalysts," *Applied Catalysis A: General,* vol. 338, no. 1, pp. 136-146, 2008.

[61] H. Tanaka, R. Kaino, K. Okumura, T. Kizuka, Y. Nakagawa, and K. Tomishige, "Comparative study of Rh/MgO modified with Fe, Co or Ni for the catalytic partial oxidation of methane at short contact time. Part I: Characterization of catalysts," *Applied Catalysis A: General,* vol. 378, no. 2, pp. 175-186, 2010.

[62] J. Greeley and M. Mavrikakis, "Surface and Subsurface Hydrogen: Adsorption Properties on Transition Metals and Near-Surface Alloys," *The Journal of Physical Chemistry B,* vol. 109, no. 8, pp. 3460-3471, 2005.

[63] F. Bozso, G. Ertl, M. Grunze, and M. Weiss, "Chemisorption of hydrogen on iron surfaces," *Applications of Surface Science,* vol. 1, no. 1, pp. 103-119, 1977.

[64] X. Lin *et al.*, "Carbon dioxide reforming of methane over Ni catalysts prepared from Ni-Mg-Al layered double hydroxides: Influence of Ni loadings," vol. 162, pp. 271-280, 2015.

[65] A. Djaidja, H. Messaoudi, D. Kaddeche, and A. Barama, "Study of Ni–M/MgO and Ni–M–Mg/Al (M=Fe or Cu) catalysts in the CH4–CO2 and CH4–H2O reforming," *International Journal of Hydrogen Energy,* vol. 40, no. 14, pp. 4989-4995, 2015.

[66] L. Jinxiang, Y. Lixin, and J. Xuanzhen, "A study of the effect of calcination temperature on the interaction between the active component and the carrier of a catalyst using thermoanalysis and X-ray diffraction," *Thermochimica Acta,* vol. 178, pp. 9-17, 1991.

[67] G. Wang, Y. Jin, G. Liu, and Y. Li, "Production of Hydrogen and Nanocarbon from Catalytic Decomposition of Methane over a Ni–Fe/Al2O3 Catalyst," *Energy & Fuels,* vol. 27, no. 8, pp. 4448-4456, 2013.

[68] X. Ge, M. Li, and J. Shen, "The Reduction of Mg–Fe–O and Mg–Fe–Al–O Complex Oxides Studied by Temperature-Programmed Reduction Combined with in Situ Mössbauer Spectroscopy," *Journal of Solid State Chemistry,* vol. 161, no. 1, pp. 38-44, 2001.

[69] S. Abelló, E. Bolshak, and D. Montané, "Ni–Fe catalysts derived from hydrotalcite-like precursors for hydrogen production by ethanol steam reforming," *Applied Catalysis A: General,* vol. 450, pp. 261-274, 2013.

[70] H. Muroyama, R. Nakase, T. Matsui, and K. Eguchi, "Ethanol steam reforming over Ni-based spinel oxide," *International Journal of Hydrogen Energy,* vol. 35, no. 4, pp. 1575-1581, 2010.

[71] D. C. Carvalho, N. A. Ferreira, J. M. Filho, O. P. Ferreira, J. M. Soares, and A. C. Oliveira, "Ni–Fe and Co–Fe binary oxides derived from layered double hydroxides and their catalytic evaluation for hydrogen production," *Catalysis Today,* vol. 250, pp. 155-165, 2015.

[72] J. I. Di Cosimo, V. K. Díez, M. Xu, E. Iglesia, and C. R. Apesteguía, "Structure and Surface and Catalytic Properties of Mg-Al Basic Oxides," *Journal of Catalysis,* vol. 178, no. 2, pp. 499-510, 1998.

[73] G. Wu, X. Wang, W. Wei, and Y. Sun, "Fluorine-modified Mg–Al mixed oxides: A solid base with variable basic sites and tunable basicity," *Applied Catalysis A: General,* vol. 377, no. 1, pp. 107-113, 2010.

[74] P. Mars and D. W. Van Krevelen, "Oxidations carried out by means of vanadium oxide catalyts," *Special Supplement to Chemical Engineering Science,* vol. 3, p. 41, 1954.

[75] T. Margossian, K. Larmier, S. M. Kim, F. Krumeich, C. Müller, and C. Copéret, "Supported Bimetallic NiFe Nanoparticles through Colloid Synthesis for Improved Dry Reforming Performance," *ACS Catalysis,* vol. 7, no. 10, pp. 6942-6948, 2017.

[76] H. Seo, "Recent Scientific Progress on Developing Supported Ni Catalysts for Dry (CO2) Reforming of Methane," *Catalysts,* vol. 8, no. 3, p. 110, 2018.

[77] N. Abdel Karim Aramouni, J. Zeaiter, W. Kwapinski, and M. N. Ahmad, "Thermodynamic analysis of methane dry reforming: Effect of the catalyst particle size on carbon formation," *Energy Conversion and Management,* vol. 150, pp. 614-622, 2017.

[78] K. O. Christensen, D. Chen, R. Lødeng, and A. Holmen, "Effect of supports and Ni crystal size on carbon formation and sintering during steam methane reforming," *Applied Catalysis A: General,* vol. 314, no. 1, pp. 9-22, 2006.

[79]   D. Kang, H. S. Lim, and J. W. Lee, "Enhanced catalytic activity of methane dry reforming by the confinement of Ni nanoparticles into mesoporous silica," *International Journal of Hydrogen Energy,* vol. 42, no. 16, pp. 11270-11282, 2017.

APPENDIX: CALCULATION FOR CATALYST SYNTHESIS

The chemical formula of hydrotalcite-derived catalyst is $\left[M_{1-x}^{2+}M_x^{3+}(OH)_2\right]^{x+}A_{x/n}^{n-}.mH_2O$. After calcination and reduction, the catalysts contain Ni-Fe/MgO-Al$_2$O$_3$. The compositions are calculated as follows. Define a = mol of Ni^{2+}, b = mol of Fe^{3+}, c = mol of Mg^{2+}, d = mol of Al^{3+}.

- For $\dfrac{M^{2+}}{M^{3+}} = 3 \Leftrightarrow \dfrac{a+c}{b+d} = 3$

The ratio of trivalent ion x is in the range of 0.2 to 0.4 to form hydrotalcite with good crystallinity. Here, $x = 0.25$.

$$x = b + d = 0.25$$
$$1 - x = a + c = 0.75$$

- The weight fraction of Ni is 20%.

$$w_{Ni} = \frac{m_{Ni}}{m_{Ni} + m_{Fe} + m_{MgO} + m_{Al_2O_3}} = \frac{a \times M_{Ni}}{a \times M_{Ni} + b \times M_{Fe} + c \times M_{MgO} + \dfrac{d}{2} \times M_{Al_2O_3}} = 20\%$$

- Molar ratio of Fe/Ni is varied, called as R

$$\frac{n_{Fe^{3+}}}{n_{Ni^{2+}}} = \frac{b}{a} = \{0; 0.1; 0.2; 0.5; 1\} = R$$

- From those equation above, a can be found as

$$\frac{a \times M_{Ni}}{a \times M_{Ni} + Ra \times M_{Fe} + (0.75 - a) \times M_{MgO} + \dfrac{(0.25 - Ra)}{2} \times M_{Al_2O_3}} = 20\%$$

$$\Leftrightarrow a = \frac{0.15 \times M_{MgO} + 0.025 \times M_{Al_2O_3}}{0.8 \times M_{Ni} - 0.2R \times M_{Fe} + 0.2 \times M_{MgO} + 0.1R \times M_{Al_2O_3}}$$

The stoichiometric coefficient of the material components was calculated in Table A1 below.

Table A1. Stoichiometric coefficient of hydrotalcite-derived catalysts

Catalyst	Stoichiometric coefficients					
	Ni^{2+}	Fe^{3+}	Mg^{2+}	Al^{3+}	OH$^-$	CO$_3^{2-}$
NiFe-1	0.159	0.159	0.591	0.091	2	0.125
NiFe-0.5	0.158	0.079	0.592	0.171	2	0.125
NiFe-0.2	0.157	0.031	0.593	0.219	2	0.125
NiFe-0.1	0.157	0.016	0.593	0.234	2	0.125
NiFe-0.1-FA	0.157	0.016	0.593	0.234	2	0.125

NiFe-0.1-F	0.157	0.016	0.593	0.234	2	0.125
NiFe-0	0.156	0.000	0.594	0.250	2	0.125

For the synthesis by conventional method, the total metal concentration of 400-mL metal nitrate solution was 0.5 M. For the synthesis by fast injection method, the total metal concentration of 100-mL metal nitrate solution was 0.25 M. Moreover, one equivalent of Na_2CO_3 was excessively added to ensure pillaring. Hence, based on the stoichiometric coefficient of the components, the mass of the salts needed for catalyst synthesis was calculated and showed as Table A.2 below.

Table A.2. Mass of the salts used for catalyst synthesis

Catalyst	Mass of the reactants (g)					
	$Ni(NO_3)_2.6H_2O$	$Fe(NO_3)_3.9H_2O$	$Mg(NO_3)_2.6H_2O$	$Al(NO_3)_3.9H_2O$	NaOH	Na_2CO_3
NiFe-1	9.2584	12.8604	30.2983	6.8137	16.0000	5.2995
NiFe-0.5	9.1717	6.3700	30.3747	12.8410	16.0000	5.2995
NiFe-0.2	9.1195	2.5335	30.4208	16.4038	16.0000	5.2995
NiFe-0.1	9.1124	1.2658	30.4270	17.5811	16.0000	5.2995
NiFe-0	9.0964	0.0000	30.4411	18.7565	16.0000	5.2995
NiFe-0.1-FA	1.1390	0.1582	3.8034	2.1976	2.0000	0.6624
NiFe-0.1-F	1.1390	0.1582	3.8034	2.1976	2.0000	0.6624